Chem Soc Rev

π-Conjugated bis(terpyridine)metal complex molecular wires

Journal:	*Chemical Society Reviews*
Manuscript ID:	CS-REV-01-2015-000081.R1
Article Type:	Review Article
Date Submitted by the Author:	19-Mar-2015
Complete List of Authors:	Sakamoto, Ryota; The University of Tokyo, Department of Chemistry, Graduate School of Science Wu, Kuo-Hui; University of Tokyo, Department of Chemistry Matsuoka, Ryota; University of Tokyo, Department of Chemistry Maeda, Hiroaki; University of Tokyo, Department of Chemistry Nishihara, Hiroshi; University of Tokyo, Department of Chemistry

Journal Name

RSCPublishing

ARTICLE

π-Conjugated bis(terpyridine)metal complex molecular wires

Cite this: DOI: 10.1039/x0xx00000x

Ryota Sakamoto,* Kuo-Hui Wu, Ryota Matsuoka, Hiroaki Maeda and Hiroshi Nishihara*

Received 00th January 2012,
Accepted 00th January 2012

DOI: 10.1039/x0xx00000x

www.rsc.org/

Bottom-up approaches have gained significant attention recently for the creation of nano-sized, ordered functional structures and materials. Stepwise coordination techniques, in which ligand molecules and metal sources are reacted alternatively, offer several advantages. Coordination bonds are stable, reversible, and self-assembling, and the resultant metal complex motifs may contain functionalities unique to their own characteristics. This review focuses on metal complex wire systems, specifically the bottom-up fabrication of linear and branched bis(terpyridine)metal complex wires on electrode surfaces. This system possesses distinct and characteristic electronic functionalities, intra-wire redox conduction and excellent long-range electron transport ability. This series of comprehensive studies exploited the customizability of bis(terpyridine)metal complex wires, including examining the influence of building blocks. In addition, simple yet effective electron transfer models were established for redox conduction and long-range electron transport. A fabrication technique for an ultra-long bis(terpyridine)metal complex wire is also described, along with its properties and functionality.

1. Introduction

Bottom-up methods[1] are useful in the fabrication of nano-sized, ordered structures, which are constructed from tiny components (e.g., atoms, ions, molecules, or nanoparticles). One of the advantages of the bottom-up method is the realization of tailor-made molecular systems using layer-by-layer techniques,[2] in which substrates modified with self-assembled monolayers (SAMs) or polymers are used as scaffolds. In the layer-by-layer protocol, two or more components are deposited sequentially and repeatedly to elongate the multilayer in a controlled manner. Examples of this technique include click chemistry between azides and terminal alkynes,[3] dehydration between aldehydes and amines to form imines,[4] and electrostatic interactions.[5]

Ryota Sakamoto was born in Yamagata Vil., Nagano, Japan in 1980. He graduated from The University of Tokyo (Japan) in 2002, and received his Ph.D. degree from the same university in 2007 under the supervision of Prof. Hiroshi Nishihara. Then he was appointed as an assistant professor at Tokyo University of Science (Japan), working with Prof. Takeshi Yamamura. In 2010 he moved to The University of Tokyo, joining Prof. Nishihara's group again. His current research interest lies on the construction of molecule-based nanostructures, and photonic and electronic devices using thereof.

Hiroshi Nishihara received his B. Sc. Degree in 1977, M. Sc. in 1979 and D. Sc. in 1982 from The University of Tokyo. He was appointed research associate of Department of Chemistry at Keio University in 1982, and he was promoted lecturer in 1990, and associate professor in 1992. Since 1996, he has been a professor of Department of Chemistry, School of Science at The University of Tokyo. He also worked as a visiting research associate of Department of Chemistry at The University of North Carolina at Chapel Hill (1987-1989), and as a researcher of PRESTO, JST (1992-1996). He received The Chemical Society of Japan Award for Creative Work in 2003, Docteur Honoris Causa from University of Bordeaux in 2011, and Commendation for Science and Technology by MEXT in 2014.

The stepwise construction of multilayer structures using coordination reactions (Fig. 1) has significant synthetic utility

because coordination bonds strike a good balance between robustness and reversibility. Coordination reactions often undergo spontaneous and quantitative conjugation between metal sources and ligand molecules that may produce defectless self-assembled multilayers. The role that coordination reactions and bonds play is not limited to the connection of neighbouring layers. In addition, resultant metal complex motifs can impart their inherent functionalities, such as redox properties, magnetism, emission, catalytic activities, and intermetallic interactions. Various combinations of metal ions and ligand molecules have been employed in the stepwise coordination architecture: Zr(IV) and Ti(IV)/phosphoric, carboxylic, and hydroxamic acid,[6] Pd(II), Ag(I) and Cu(II)/pyridine,[7] and

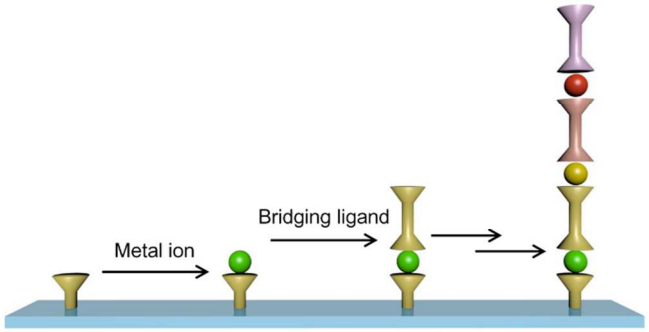

Fig. 1 Stepwise coordination process on a substrate surface.

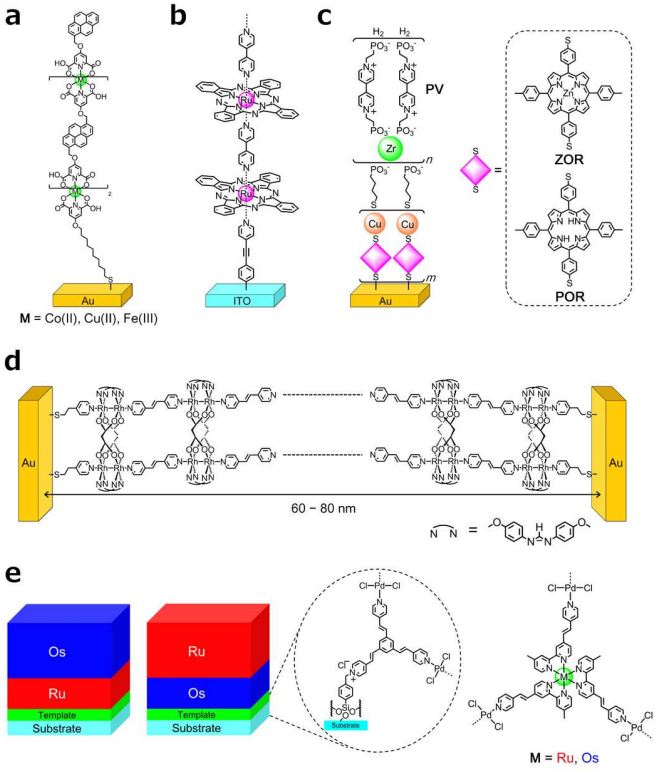

Fig. 2 (a-c) Examples of metal complex multilayers for photocurrent generation. (d) Example of molecular wiring. (e) Example of a redox film showing charge trapping.

others.[8] Typically, metal ions generated from metal salts are used as the metal source, but metal complexes and metal clusters may also participate in the layer-by-layer protocols (i.e., ruthenium-coordinated phthalocyanine[9] and trinuclear ruthenium clusters).[9-11]

Lambert and McGimpsey's group evaluated the effect of metal ions on photocurrent response.[12] They prepared a pyrene-containing multilayer using copper(II), cobalt(II), and iron(III) (Fig. 2a) and measured the photocurrent generation ability in the presence of methyl viologen and triethanolamine for cathodic and anodic currents, respectively. The largest cathodic photocurrent was observed in the copper(II) system, and the iron(III) complex system exhibited the greatest anodic photocurrent. Dong and co-workers investigated the influence of the number of the layers on photocurrent generation using the system shown in Fig. 2b[9,10,13] and found that thicker layers generated smaller photocurrents because of the internal resistance of the molecular wire. Thompson et al. fabricated porphyrin-viologen conjugate films using copper(II) and zirconium(IV) (Fig. 2c).[14] They prepared three types of multilayer systems: POR_3/PV_3, ZOR_3/PV_3 and mixed-porphyrinic ZOR_2POR/PV_3. Their quantum yields for photocurrent generation were estimated to be 2.4%, 2.3%, and 3.5% for POR_3/PV_3, ZOR_3/PV_3, and ZOR_2POR/PV_3, respectively. The authors ascribed the higher efficiency in the mixed-porphyrinic film to redox potential arrays suitable for charge separation. Lin and Kagan tethered a gold electrode gap of 60–80 nm with a rhodium cluster wire prepared by the stepwise coordination method (Fig. 2d).[15] In the resultant $I - V$ curves, the first scan showed a negative differential resistance. The authors speculated that this negative differential resistance is derived from the oxidation of the rhodium cluster unit. Charge trapping behaviour was reported in hetero-metal complex films created by van der Boom et al. (Fig. 2e).[16] An osmium complex layer formed on an 8.0-nm-thick ruthenium complex layer showed a sharp catalytic oxidation peak without a prominent reduction wave, whereas the ruthenium complex layer produced a reversible redox wave. Conversely, a ruthenium complex layer fabricated on a thick osmium complex layer exhibited a sharp reduction peak and deformed oxidation wave, whereas a reversible redox couple of the osmium complex layer appeared. This series of phenomena can be explained by electron transport between the top layer and electrode through the bottom-layer.

The present review summarizes progress in metal complex molecular wires in the last decade,[17] covering fabrication procedures for linear and branched oligomer wires, characteristic intra-wire redox conduction, excellent long-range electron transport ability in the linear wire, and elucidation of the long-range electron transport ability in the branched wire through an effective model. In addition, an ultra-long metal complex wire based the bis(terpyridine)metal complex motif[18] is reported.

2. Precise synthesis of linear and branched bis(terpyridine)metal complex wires: intra-wire redox conduction and superior electron transport ability

2.1 Fabrication and analytical procedures

Fig. 3 illustrates the fabrication procedure for a series of bis(terpyridine)metal complex wires. Mica deposited with gold and silicon(111) was used as a substrate. It is important to prepare clean surfaces prior to the growth of molecular wires.

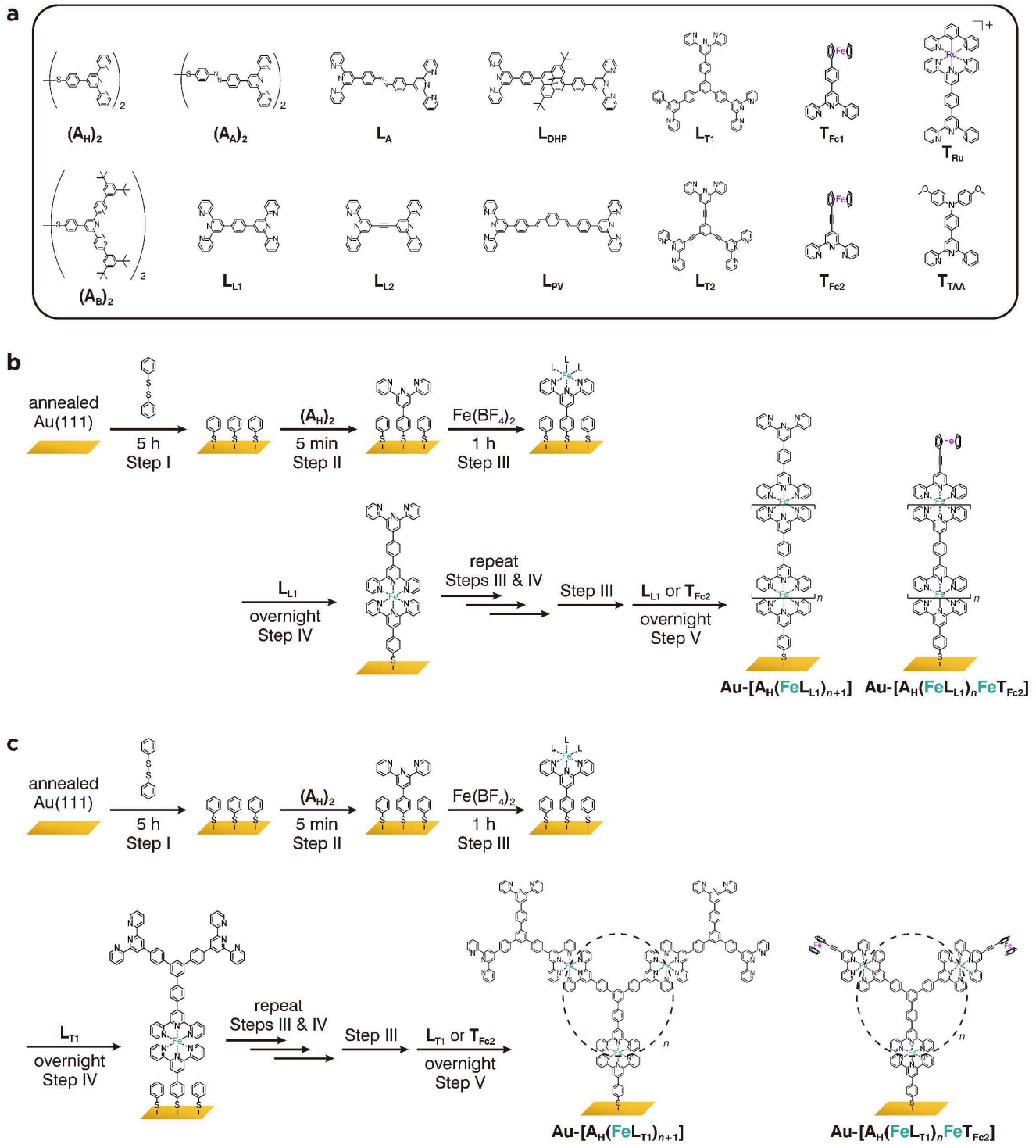

Fig. 3. (a) Constitutive components for bis(terpyridine)metal complex wires. (b) Stepwise coordination procedure for the preparation of Au-$[A_H(FeL_{L1})_{n+1}]$ and Au-$[A_H(FeL_{L1})_nFeT_{Fc2}]$. Step I: diphenyl disulfide in chloroform; Step II: surface anchor ligand $(A_H)_2$ in chloroform; Step III: $Fe(BF_4)_2$ in ethanol; Step IV: bridging ligand L_{L1} in chloroform; Step V: terminal ligand T_{Fc2} in chloroform. (c) Stepwise coordination procedure for the preparation of Au-$[A_H(FeL_{T1})_{n+1}]$ and Au-$[A_H(FeL_{T1})_nFeT_{Fc2}]$. Step I: diphenyl disulfide in chloroform; Step II: surface anchor ligand $(A_H)_2$ in chloroform; Step III: $Fe(BF_4)_2$ in ethanol; Step IV: three-way ligand L_{L1} in chloroform; Step V: terminal ligand T_{Fc2} in chloroform.

The former was annealed with a hydrogen flame, exposing the Au(111) surface. The latter was immersed in aqueous HF or NH_4F to yield a hydrogen-terminated Si(111) surface.

The bis(terpyridine)metal complex wire consisted of four components: a surface-anchor terpyridine ligand (**A** series), metal ions, a bridging terpyridine ligand (**L** series), and a redox-active terminal terpyridine ligand (**T** series) (Fig. 3a). These diverse components facilitated the construction of various types of molecular wires. The construction of the linear bis(terpyridine)iron(II) complex wires, Au-$[\mathbf{A_H(FeL_{L1})}_{n+1}]$ and $[\mathbf{A_H(FeL_{L1})}_n\mathbf{FeT_{Fc1}}]$ (Fig. 3b), was initiated by SAM formation on the substrate surface using diphenyl disulphide and $\mathbf{A_H}$ (steps 1 and 2). The gold-thiol protocol[19] was used for the Au(111) surface. The former wire was thinner with a reduced density, thereby being optional. The Au substrate was immersed in a chloroform solution of disulphide-terpyridine $(\mathbf{A_H})_2$. The series of SAM formation procedures yielded a terpyridine-terminated surface, which served as a scaffold for the bis(terpyridine)metal complex wires. Growth of the molecular wire depended on the stepwise coordination technique.[20] To implant Fe^{2+} ions, the substrate modified with the terpyridine scaffold $\mathbf{A_H}$ was immersed in an ethanol solution of $Fe(BF_4)_2$ (step 3). The metal-terminated surface was then immersed in a chloroform solution of $\mathbf{L_{L1}}$ to complete the bis(terpyridine)iron(II) complex motif (step 4). Steps 3 and 4 were repeated n+1 times to prepare Au-$[\mathbf{A_H(FeL_{L1})}_{n+1}]$. The final implantation of $\mathbf{L_{L1}}$ may be substituted with $\mathbf{T_{Fc1}}$ (step 5) to generate Au-$[\mathbf{A_H(FeL)}_n\mathbf{FeT}]$. This process makes decoration of the tip of the bis(terpyridine)iron(II) wire with redox-active functional groups, such as ferrocene, triarylamine, and cyclometallated ruthenium(II) complexes, possible. These groups guide investigations into long-range electron transport ability (vide infra). Cobalt ions can serve as the metal centre, if the metal source is substituted with $[Co(NH_3)_6]Cl_3$. In addition, the authors fabricated several mixed-metal wires with different compositions and orders. Construction of branched bis(terpyridine)iron(II) wires Au-$[\mathbf{A_H(FeL_{T1})}_{n+1}]$ was the same as that of the linear wire, except that the bridging terpyridine ligand was replaced with a three-way terpyridine ligand $\mathbf{L_{T1}}$ (Fig. 3c). The terminus of the branched molecular wire may also be modified with **T** (e.g., Au-$[\mathbf{A_H(FeL_{T1})}_n\mathbf{FeT_{Fc1}}]$).

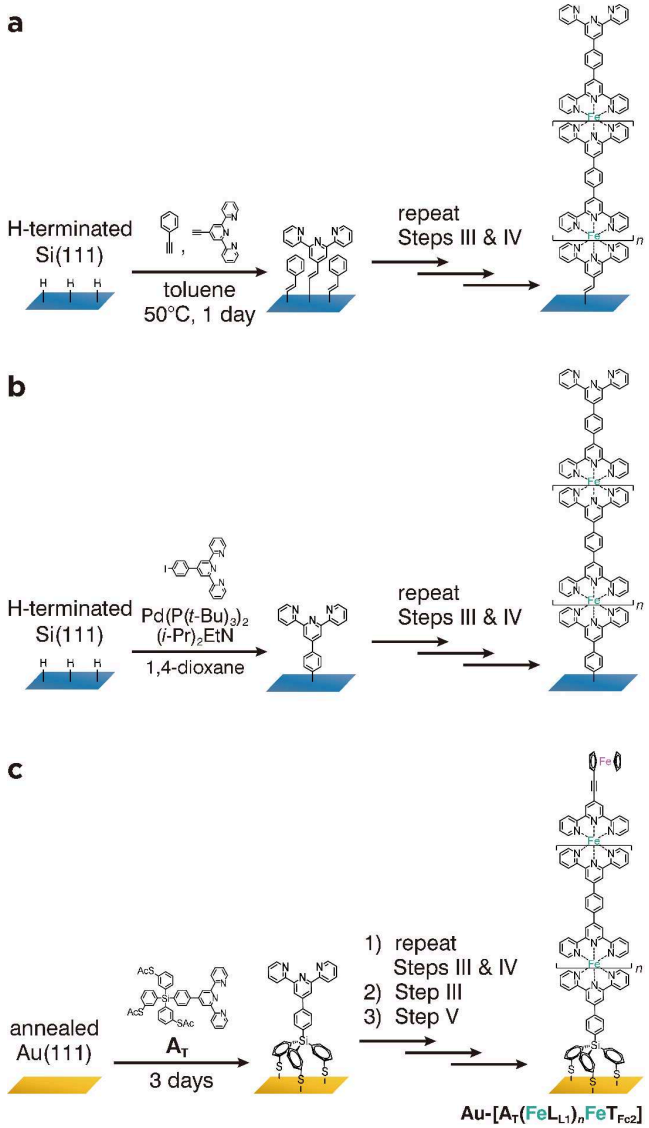

Fig. 4 Fabrication procedures for bis(terpyridine)iron(II) complex wires on Si(111) substrates (a) anchored by an ethenylene linker. (b) anchored by phenylene linker. (c) Fabrication procedure for Au-$[\mathbf{A_T(FeL_{L1})}_n\mathbf{FeT_{Fc2}}]$.

A hydrogen-terminated Si(111) surface was modified using a hydrosilylation protocol.[21] Herein, the surface was reacted in toluene with terpyridine that has a terminal acetylene, which leaves a terpyridine scaffold tethered to an ethenylene linkage (Fig. 4a). The substrate may be pretreated with ethynylbenzene as a thinner. An innovative type of Pd-catalysed arylation was applied to hydrosilanes.[22] Bis(terpyridine)iron(II) wires with phenylene linkers were prepared by applying the reaction to the hydrogen-terminated Si(111) surface (Fig. 4b). The same processes used to produce a Au(111) surface (i.e., steps 2-5 in Fig. 3b, c) may be applied for the elongation of the molecular wire. A Si(111) surface advantageously affords the molecular wire with an orthogonal configuration, whereas a Au(111) surface is tilted by the nature of the Au-S bond. The authors also designed and synthesized a tripodal terpyridine scaffold for a Au(111) surface (Fig. 4c) that produced orthogonal molecular wires. In all, the bottom-up coordination procedure yielded various types of bis(terpyridine)metal complex wires with desired compositions and structures.

Molecular wires fabricated on the substrate surface were analysed by cyclic voltammetry (Fig. 5a-d), XPS (Fig. 6), cross-sectional SEM (Fig. 7a), STM (Fig. 7b), and AFM (Fig. 7c, d). Fig. 5a, b shows typical cyclic voltammograms for linear and branched $Fe(tpy)_2$ molecular wires, Au-$[\mathbf{A_A(FeL_{L1})}_{n+1}]$ and Au-$[\mathbf{A_A(FeL_{T2})}_{n+1}]$, respectively. The redox peak of the $[Fe(tpy)_2]^{3+}/[Fe(tpy)_2]^{2+}$ couple was observed at approximately 0.65 V versus ferrocenium/ferrocene (Fc^+/Fc), which increased as generation n grew (tpy = 2,2':6',2''-terpyridine). Fig. 5c shows the surface coverage of the $Fe(tpy)_2$ unit, Γ[Fe], calculated from the cyclic voltammograms. In the linear wire, Γ was proportional to n, which ensured that the growth of the $Fe(tpy)_2$ molecular wire was quantitative. From a geometric point of view, Γ[Fe] was proportional to $2^{n+1}-1$ in the branched wire. However, this relationship was only valid up to n = 3, and Γ[Fe] began to saturate thereafter. This discrepancy stems from steric repulsion among the dendrons of the $Fe(tpy)_2$ molecular wire and/or between the wire and electrode surface. Fig. 5d shows typical cyclic voltammograms of the linear bis(terpyridine)iron(II) complex wire Au-$[\mathbf{A_H(FeL_{L1})}_n\mathbf{FeT_{Fc2}}]$, where redox-active ferrocene was placed at the wire terminus. Redox waves of both $[Fe(tpy)_2]^{3+}/[Fe(tpy)_2]^{2+}$ and

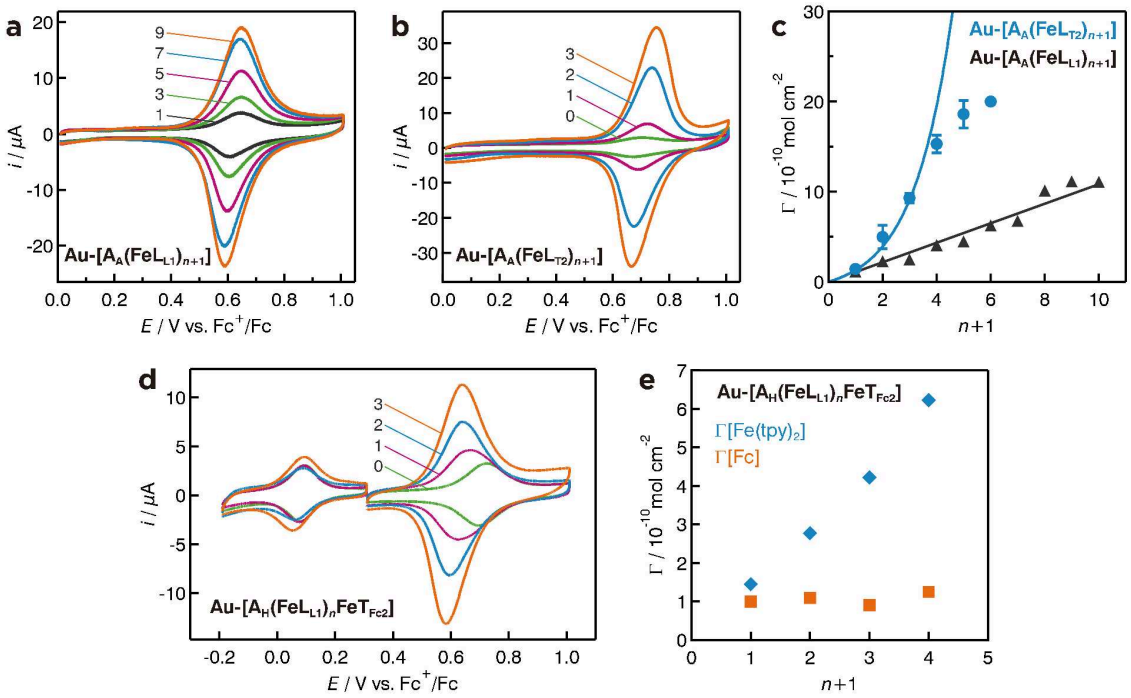

Fig. 5 Cyclic voltammograms of (a) Au-$[\mathbf{A_A(FeL_{L1})}_{n+1}]$ (n = 1, 3, 5, 7, and 9) and (b) Au-$[\mathbf{A_A(FeL_{T2})}_{n+1}]$ (n = 0–3) at a scan rate of 0.1 V s^{-1} in 1 M Bu_4NClO_4/CH_2Cl_2. (c) Surface coverage (Γ[Fe(tpy)$_2$])–generation (n+1) plots for Au-$[\mathbf{A_A(FeL_{L1})}_{n+1}]$ and Au-$[\mathbf{A_A(FeL_{T2})}_{n+1}]$ (tpy = 2,2′:6′,2″-terpyridine). Γ[Fe(tpy)$_2$] is calculated from the anodic peak area of the cyclic voltammogram. (d) Cyclic voltammograms of Au-$[\mathbf{A_H(FeL_{L1})}_n\mathbf{FeT_{Fc2}}]$ (n = 0–3) in 1 M Bu_4NClO_4/CH_2Cl_2. (e) Surface coverages (Γ[Fe] and Γ[Fc])–generation (n+1) plots for Au-$[\mathbf{A_H(FeL_{L1})}_n\mathbf{FeT_{Fc2}}]$. Γ[Fe(tpy)$_2$] (blue) and Γ[Fc] (orange) are calculated from the anodic peak area of the cyclic voltammogram. Adapted with permission from ref. 17b,h. Copyright 2007, 2013 Wiley-VCH Verlag GmbH&Co. KGaA.

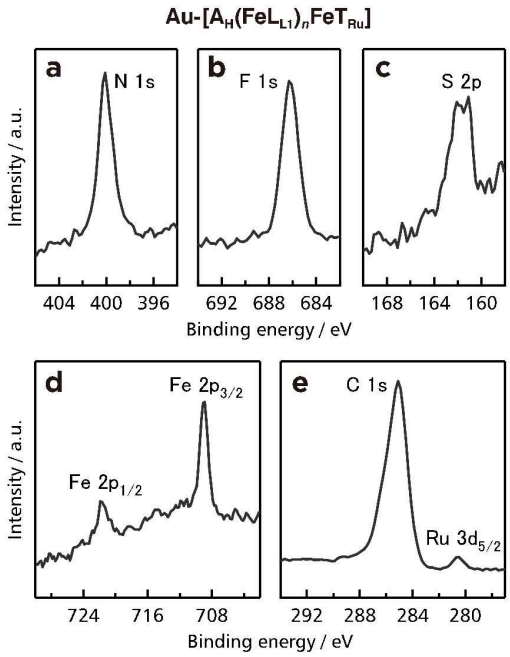

Fig. 6 X-ray photoelectron spectra for Au-$[\mathbf{A_H(FeL_{L1})}_n\mathbf{FeT_{Ru}}]$ at an exit angle of 45°. a) N 1s, b) F 1s, c) S 2p, d) Fe 2p, and e) C 1s and Ru 3d. Adapted with permission from ref. 17h. Copyright 2013 Wiley-VCH Verlag GmbH&Co. KGaA.

ferrocene$^+$/ferrocene (0.08 V) were observed, and surface coverage reflected the structural features of the molecular wires (Fig. 5e). Γ[Fe(tpy)$_2$] was proportional to n, whereas the surface coverage of the ferrocene moiety, Γ[Fc], was constant.

X-ray photoemission spectroscopy (XPS) provides information on constitutive elements. Au-$[\mathbf{A_H(FeL_{L1})}_n\mathbf{FeT_{Ru}}]$ contained peaks derived from N 1s (binding energy: 400.1 eV), F 1s (686.7 eV), S 2p (161.5 eV), and Fe 2p ($2p_{3/2}$: 709.1 eV and $2p_{1/2}$: 721.9 eV). Fluorine is derived from BF_4^-, the counter anion of the Fe(tpy)$_2$ unit (Fig. 6). The peak corresponding to Ru $3d_{5/2}$ (280.9 eV) stems from the terminal cyclometallated ruthenium(II) complex.

A series of microscopic techniques described the nanostructures in the bis(terpyridine)metal complex wires. Cross-sectional scanning electron microscopy (SEM) of linear Au-$[\mathbf{A_A(CoL_A)_{47}}]$ revealed a dense film on the cobalt complex wires with a thickness of ca. 100 nm (Fig. 7a), which is also the estimated height of the molecular wires. A representative scanning tunnelling microscopic (STM) image of branched Au-$[\mathbf{A_H(FeL_{T1})_2FeT_{Fc2}}]$ is shown in Fig. 7b, which features sparsely placed cylindrical structures. The diameter of the top face of the cylinder was ca. 5 nm, consistent with the size of the branched molecular wire. Atomic force microscopy (AFM) of the orthogonal linear wire Au-$[\mathbf{A_T(FeL_{L1})_5}]$ (Fig. 7c,d) showed a dip that formed by scratching the modified Au(111) surface with an AFM tip, and cross-sectional analysis assigned it a depth of 9–10 nm. This value is also consistent with the estimated height of Au-$[\mathbf{A_T(FeL_{L1})_5}]$.

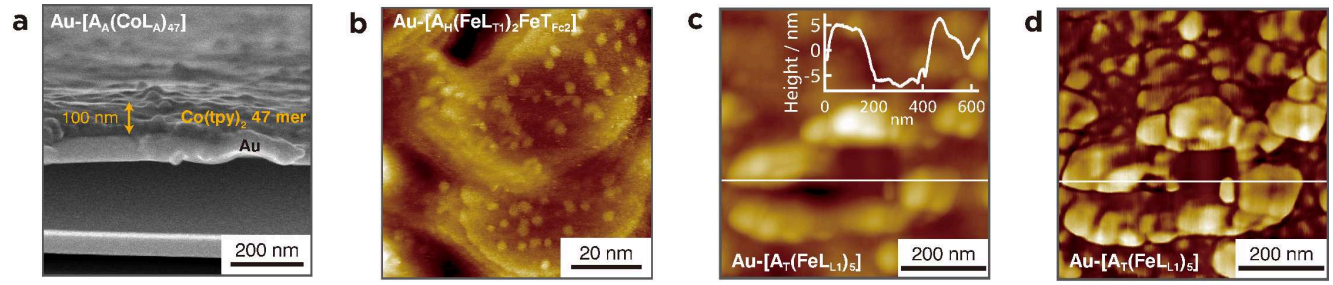

Fig. 7 (a) Cross-sectional SEM image for Au-**[$A_A(CoL_A)_{47}$]**. (b) Representative STM image of Au-**[$A_H(FeL_{T1})_2FeT_{Fc2}$]** (75 × 75 nm^2). AFM (c) height and (d) phase images of Au-**[$A_T(FeL_{L1})_5$]** after scratching using an AFM tip. The white dashed squares indicate the scratched area. (c ,inset) Cross-sectional analysis for image (c) at the intersecting white line. Adapted with permission from ref. 17a,g,k. Copyright 2005 The Chemical Society of Japan, 2013 The Royal Society of Chemistry, and 2015 American Chemical Society.

2.2 Intra-wire redox conduction

Electron-conducting oligomer/polymer wires have recently gained attention in the field of molecular electronics. Redox polymers, in which redox species are connected to form polymer strands, are representative electron-conducting materials,[23] yet there have been no detailed studies on electron transfer within a single redox-polymer wire. The early stages of modified electrode research began in 1970s. Since then, most electrode surfaces have been coated with redox-polymers by means of polymer coating, chemical modification, and electrochemical polymerisation, and then subjected to experimental and theoretical investigations on electron transport.[24] In these systems, the polymer strands were randomly distributed, with electron transport phenomena based on "redox conduction".[25] In this scheme, the diffusional motions of collective electron-transfer pathways play a primary role. The apparent diffusion coefficient (D_{app}) for electron transport is composed of electron-hopping and/or physical diffusion terms and is the key factor in the Dahms-Ruff equation[26] and Laviron-Andrieux-Savéant theory.[27] The migration effect and counter-ion motion are also important with respect to D_{app}.[28]

Our bis(terpyridine)metal complex wire featured a rigid structure that was perpendicular to the electrode surface (Figs. 3, 4). We expect that it undergoes redox electron transport based on a mechanism different from conventional polymer films with random compositions and structures. To clarify the "intra-wire redox conduction" phenomenon in the bis(terpyridine)iron(II) complex wire, we adopted potential-step chronoamperometry (PSCA) to branched Au-**[$A_A(FeL_{T2})_{n+1}$]** and linear Au-**[$A_A(FeL_{L1})_{n+1}$]**. Fig. 8 shows the PSCA results. Throughout the experiments, the applied potential was varied from 0.96 to 0.36 V, such that the valences of all $Fe(tpy)_2$ units (formal potential: ca. 0.65 V) were reduced from +3 to +2. If redox conduction is dominated by diffusional motion and the diffusion process within the film is the rate-determining step (i.e., electron transfer between the electrode and the nearest redox sites in the film is sufficiently fast), an PSCA (i.e., i_{exp} - t plot) of a reduction reaction will obey the Cottrell equation (1):

$$i_{exp} = -nFAD_{app}^{1/2} C (\pi t)^{-1/2} + i_{DL} \quad (1)$$

where n, F, A, C, and i_{DL} describe the number of electrons, Faraday constant, electrode area, concentration of the redox species in the film, and charging current to the electric double layer, respectively. Thus, the first term corresponds to the faradaic current for the reduction. Because i_{DL} tends to decay

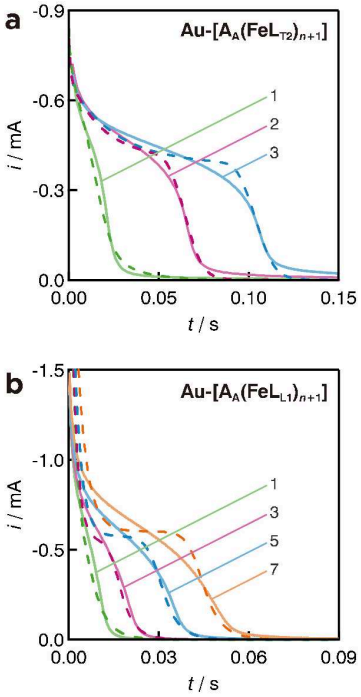

Fig. 8 Experimental (solid lines) and reproduced (dashed lines) potential step chronoamperograms of (a) branched wire Au-**[$A_A(FeL_{T2})_{n+1}$]** (n = 1, 2, and 3) (b) linear wire Au-**[$A_A(FeL_{L1})_{n+1}$]** (n = 1, 3, 5, and 7) in 1 M Bu_4NClO_4/dichloromethane with a potential step from 0.96 to 0.36 V. The potential step affords reduction to all $[Fe(tpy)_2]^{3+}$ species into $[Fe(tpy)_2]^{2+}$. Reproduced PSCAs are obtained by means of numerical simulation based on the intrawire redox hopping mechanism shown in Fig. 9, and eqs. (3) and (4) thereof. Used parameters are as follows. (a) k_{-1} = 270 s^{-1}, k_{-2} = 3.8 × 10^2 s^{-1}, C_{dl} = 8.3 μF for Au-**[$A_A(FeL_{T2})_2$]**; k_{-1} = 270 s^{-1}, k_{-2} = 3.9 × 10^2 s^{-1}, C_{dl} = 8.3 μF for Au-**[$A_A(FeL_{T2})_3$]**; k_{-1} = 260 s^{-1}, k_{-2} = 3.5 × 10^2 s^{-1}, C_{dl} = 12 μF for Au-**[$A_A(FeL_{T2})_4$]**. (b) k_{-1} = 220 s^{-1}, k_{-2} = 2.3 × 10^3 s^{-1}, C_{dl} = 7.2 μF for Au-**[$A_A(FeL_{L1})_2$]**; k_{-1} = 260 s^{-1}, k_{-2} = 1.9 × 10^3 s^{-1}, C_{dl} = 7.1 μF for Au-**[$A_A(FeL_{L1})_4$]**; k_{-1} = 230 s^{-1}, k_{-2} = 1.3 × 10^3 s^{-1}, C_{dl} = 9.2 μF for Au-**[$A_A(FeL_{L1})_6$]**; k_{-1} = 210 s^{-1}, k_{-2} = 1.3 × 10^3 s^{-1}, C_{dl} = 13 μF for Au-**[$A_A(FeL_{L1})_8$]**. Adapted with permission from ref. 17b. Copyright 2007 Wiley-VCH Verlag GmbH&Co. KGaA.

much faster than the faradaic current, the i_{exp} - $t^{-1/2}$ plot is linear unless the diffusion layer does not reach the terminus of the film.[29] In sharp contrast, both branched and linear bis(terpyridine)iron oligomer wires did not contain straight-line regions in the i - $t^{-1/2}$ plots (data not shown). We then hypothesized that the unusual i_{exp} - t characteristics were derived from an intra-wire electron transport pathway, a sequential electron-hopping model (Fig. 9). In this new mechanism, we considered a condition in which all bis(terpyridine)iron complex sites were initially oxidized (i.e., $[Fe(tpy)_2]^{3+}$ state), and the modified electrode was cathodically

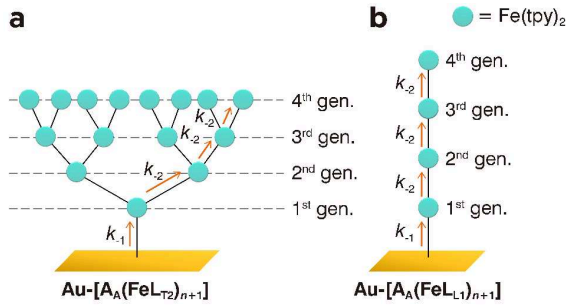

Fig. 9 Sequential electron hopping model in (a) branched wire Au-**[$A_A(FeL_{T2})_{n+1}$]** and (b) linear wire Au-**[$A_A(FeL_{L1})_{n+1}$]**. The turquoise circle denote a $Fe(tpy)_2$ unit.

polarized enough to induce the one-electron reduction of all $[Fe(tpy)_2]^{3+}$ sites to $[Fe(tpy)_2]^{2+}$. Electrons injected from the gold electrode to the bis(terpyridine)iron complex wire were propagated to the end of the wire by intra-wire hopping between the $[Fe(tpy)_2]$ sites as follows:

$$Ox_1 + e^- \rightarrow Red_1 \qquad \text{rate constant: } k_{-1} \qquad (2a)$$

$$Red_{m-1} + Ox_m \rightarrow Ox_{m-1} + Red_m \qquad \text{rate constant: } k_{-2} \quad (m = 2, 3 \ldots n+1) \qquad (2b)$$

where Ox_m and Red_m denote the $[Fe(tpy)_2]^{3+}$ and $[Fe(tpy)_2]^{2+}$ sites, respectively, at the mth generation (see Fig. 9 for the definition of the generation). The back electron transfer, such as from Red_3 to Ox_2, was likely neglected because of sufficient negative overpotential. In this scheme, a set of kinetic equations is expressed as follows:
for branched wires:

$$dP_1/dt = -2\,k_{-2}P_1(1-P_2) + k_{-1}(1-P_1) \qquad (3a)$$

$$dP_m/dt = -2k_{-2}P_m(1-P_{m+1}) + k_{-2}P_{m-1}(1-P_m) \quad (m = 2, 3, \ldots, n) \qquad (3b)$$

$$dP_{n+1}/dt = k_{-2}P_n(1-P_{n+1}) \qquad (3c)$$

for linear wires:

$$dP_1/dt = -\,k_{-2}P_1(1-P_2) + k_{-1}(1-P_1) \qquad (4a)$$

$$dP_m/dt = -\,k_{-2}P_m(1-P_{m+1}) + k_{-2}P_{m-1}(1-P_m) \quad (m = 2, 3, \ldots, n) \qquad (4b)$$

$$dP_{n+1}/dt = k_{-2}P_n(1-P_{n+1}) \qquad (4c)$$

where P_m is the electron population ratio (i.e., fraction of $[Fe(tpy)_2]^{2+}$) for the mth generation. In this scheme, the faradaic current i_F, which corresponds to the electron flux from the electrode to the $Fe(tpy)_2$ wire, is expressed as follows:

$$i_F = -FA\Gamma k_{-1}(1-P_1) \qquad (5)$$

where Γ is the surface coverage (in mol cm^{-2}) of the branched or linear wire. The simulated total current i_{sim} corresponds to the sum of i_F and the electric double layer charging current i_{DL}:

$$i_{sim} = i_F + i_{DL} \qquad (6)$$

where i_{DL} corresponds to the charging current to the electric double layer, which is dominated by solution resistance R_{sol} and capacitance C_{DL}. Therefore, the numerical simulation is equivalent to the reproduction of i_{exp} with i_{sim}, while varying the k_{-1} and k_{-2} values. The resulting i_{sim} values (shown as dashed lines) with the parameters used are given in the captions of Fig. 8 and were consistent with the experimental PSCAs, i_{exp}, for both branched and linear wires of various generations. The fact that both branched and linear wires use the same mechanism strongly supports our theory, excluding the existence of inter-wire pathways.

Redox conduction in the oligomer films occurs by the diffusional random walk mechanism, but on the through-bond electron transport. Thanks to the rigid and tunable structure of the bis(terpyridine)iron complex wire, we observed peculiar i_{exp}-t characteristics in PSCA that were reproduced by the intra-wire electron transport mechanism, where electrons hop successively between neighbouring $Fe(tpy)_2$ sites. This new type of redox-polymer film will be useful for fundamental studies on molecular electronics.

2.3 Supreme long-range electron transport ability

The question of how electrons move through a single molecular wire is of fundamental importance to molecular science, especially in the field of molecular devices and biological electron-transfer systems.[30-35] D-B-A systems are typically used to evaluate the electron transport ability of molecular wires, where D, B, and A denote an electron-donor molecule or electrode, a molecular wire in focus, and an electron-acceptor molecule or electrode, respectively. The attenuation factor β is frequently used as a measure of electron transport ability. β is associated with the first-order electron transfer rate constant from D and A (k) and the distance between D–A (d) using eq. (7):[36]

$$k = k_0 \exp(-\beta d) \qquad (7)$$

where k_0 is the zero-distance rate constant (i.e., d = 0). The improved electron transport ability corresponds to the smaller β value. Electrons may travel long distances without a significant decay in the transfer rate. Extensive studies have been devoted to developing molecular wires with small β values. Plain alkyl chains possess large β values (approximately 1 $Å^{-1}$),[37-41] which can be significantly reduced through the use of π-conjugated organic bridges. For example, oligo(phenylenevinylene) bridges (0.01-0.06 $Å^{-1}$)[42-44] and porphyrin wires (0.003 and 0.04 $Å^{-1}$)[45,46] had very small β. Several biomolecules conduct electrons efficiently, such as DNA (up to 0.2 $Å^{-1}$),[47-54] proteins, and oligopeptides (depending on the structure).[55-59] In addition, molecular wires with non-covalent interactions, such as hydrogen bonds and π-stacks, exhibit good long-range electron transport abilities.[60-62] For example, Guldi and Martín determined the long-range electron transport ability of paracyclophane-based molecular wires (0.145 $Å^{-1}$ and 0.012 $Å^{-1}$).[61]

The sequential electron-hopping mechanism is known to contribute to electron transport over long distances, whereas the superexchange (tunnelling) mechanism is only dominant over short distances.[63] In fact, Wishart and Isied found a crossover point for the two mechanisms in peptide chains comprising proline residues, with β values of 1.4 and 0.18 $Å^{-1}$ for the electron hopping and superexchange pathways, respectively.[64] The intra-wire redox conduction shown in Section 2.2 may be associated with long-range electron transport, resulting in a shallow β based on the electron-hopping mechanism. The β

value for the linear bis(terpyridine)metal complex wires equipped with a redox-active terminal terpyridine ligand **T** (e.g., Au-$[\mathbf{A_H(FeL_{L1})}_n\mathbf{FeT_{Fc1}}]$ illustrated in Fig. 3b) was quantified by electrochemistry. As shown in Fig. 5d, the redox of **T** precedes that of the $Fe(tpy)_2$ unit, indicating that the former may be a good probe for electron transport ability by applying appropriate electrode potentials. Technically, the β value is quantified by measuring the electron transfer rate k between the terminal redox site and the Au electrode for the n series and by linearizing the resultant ln$k$–d plot (d is the distance between the terminal redox site and Au electrode surface). The k values are quantified using potential step chronoamperometry (PSCA), as in Fig. 10 for Au-$[\mathbf{A_H(FeL_{L1})}_n\mathbf{FeT_{Fc2}}]$. The potential of the modified gold electrode is first maintained at 0.33 V (= $E^{0'}(\mathbf{T_{Fc1}})$ + 0.25 V), and then changed to –0.17 V (= $E^{0'}(\mathbf{T_{Fc1}})$ – 0.25 V), reducing the terminal ferrocenium to ferrocene. In sharp contrast, the valence of the $Fe(tpy)_2$ units is constant, +2, during the potential step because its redox potential is far more positive (0.63–0.64 V) than the series of electrode potentials. The right graph of Fig. 10a shows the lni_{exp}–t plot for Au-$[\mathbf{A_H(FeL_{L1})FeT_{Fc2}}]$ accompanied by linearisation. The slope is equal to $-k$. We then investigated the k values for the Au-$[\mathbf{A_H(FeL_{L1})FeT_{Fc2}}]$ series (n = 0–3) and plotted ln k versus d (Fig. 10b). The –β and k_0 values are the slope and intercept of the vertical axis, respectively, in accordance with eq. (7). From the analysis of the ln k – d plot by the linear least-squares method, β and k_0 were calculated to be 0.020±0.004 $Å^{-1}$ and 9.9 × 10^2 s^{-1}, respectively.

Each component of the bis(terpyridine)metal complex wire influenced the long-range electron transport ability (i.e., changes in β and k_0). The linear wire was composed of four components, a surface-anchor ligand **A**, bridging ligand $\mathbf{L_B}$, metal ion (Fe or Co), and redox-molecule-appended terminal ligand **T**, and the molecular wire can be regarded as a molecular circuit (Fig. 11). Fig. 12 and Table 1 give the results of this series of investigations. The anchor ligand's effects on the k_0 and β values were evaluated using three types of **A** ($\mathbf{A_A}$, $\mathbf{A_B}$, and $\mathbf{A_H}$, Fig. 3a). $\mathbf{L_{L1}}$ and $\mathbf{T_{Fc2}}$ are commonly used as bridging and terminal ligands, respectively (i.e., molecular wires Au-$[\mathbf{A_A(FeL_{L1})}_n\mathbf{FeT_{Fc2}}]$, Au-$[\mathbf{A_B(FeL_{L1})}_n\mathbf{FeT_{Fc2}}]$, and Au-$[\mathbf{A_H(FeL_{L1})}_n\mathbf{FeT_{Fc2}}]$). The ln k – d plots shown in Fig. 12a indicate that β is independent of **A**, exhibiting values of 0.014–0.024 $Å^{-1}$. Conversely, k_0 is dependent on **A**. Thus, the intrinsic long-range electron transport ability of the bis(terpyridine)metal complex wire is insensitive to **A**. Notably, $\mathbf{A_A}$ combined with an azobenzene spacer provides smoother electron transfer, which may be associated with efficient π-conjugation between the electrode and terpyridine unit.

The influence of bridging ligand **L** was investigated by comparing Au-$[\mathbf{A_A(FeL_{L1})}_n\mathbf{FeT_{Fc2}}]$, Au-$[\mathbf{A_A(FeL_{PV})}_n\mathbf{FeT_{Fc2}}]$, and Au-$[\mathbf{A_A(FeL_{L2})}_n\mathbf{FeT_{Fc2}}]$. This ligand influenced the β value significantly (Fig. 12b). The best long-range electron transport ability was observed in Au-$[\mathbf{A_A(FeL_{L1})}_n\mathbf{FeT_{Fc2}}]$ (0.015 ± 0.007 $Å^{-1}$), but the decay of the electron transfer rate was steeper in Au-$[\mathbf{A_A(FeL_{PV})}_n\mathbf{FeT_{Fc2}}]$ (0.031±0.008 $Å^{-1}$) and Au-$[\mathbf{A_A(FeL_{L2})}_n\mathbf{FeT_{Fc2}}]$ (0.070±0.020 $Å^{-1}$). A bridging ligand composed of dimethyldihydropyrene (DHP), $\mathbf{L_{DHP}}$, gave the smallest β value in a bis(terpyridine)iron(II) complex wire, Au-$[\mathbf{A_A(FeL_{DHP})}_n\mathbf{FeT_{Fc1}}]$ (0.008±0.006 $Å^{-1}$, Fig. 12c). As proposed above, the long-range electron transfer in the bis(terpyridine)metal complex wires occurs via a sequential

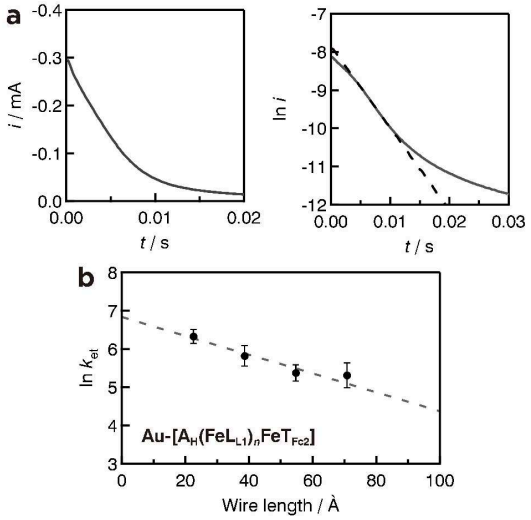

Fig. 10 (a) i_{exp}-t (left) and lni_{exp}-t (right) plots for Au-$[\mathbf{A_H(FeL_{L1})FeT_{Fc2}}]$ in 1 M TBAP/dichloromethane with a potential step from 0.33 to –0.17 V. (b) ln$k$-d plot for Au-$[\mathbf{A_H(FeL_{L1})}_n\mathbf{FeT_{Fc2}}]$ (n = 0–3). The dashed line is obtained by means of the least squares. Adapted with permission from ref. 17h. Copyright 2013 Wiley-VCH Verlag GmbH&Co. KGaA.

hopping mechanism. The DHP moiety possessed an $E^{0'}$ value (0.12 V) similar to the terminal ferrocene (0.00 V). This moiety may participate in electron hopping explicitly, thereby facilitating electron transport between the terminal ferrocene and gold electrode despite its long length.

To understand the impact of the central metal ion on β, we fabricated cobalt complex wires, Au-$[\mathbf{A_A(CoL_A)}_{n+1}\mathbf{FeL_A}]$ and Au-$[\mathbf{A_A(CoL_{L1})}_{n+1}\mathbf{FeL_{L1}}]$. The potential step in PSCA was set to 0.31 V→0.91 V for Au-$[\mathbf{A_A(CoL_A)}_{n+1}\mathbf{FeL_A}]$ and 0.91 V→0.21 V for Au-$[\mathbf{A_A(CoL_{L1})}_{n+1}\mathbf{FeL_{L1}}]$, such that the redox current of the $[Fe(tpy)_2]^{3+}/[Fe(tpy)_2]^{2+}$ couple was monitored by the valence state of the cobalt centre fixed at +3. This experiment yielded β values of 0.004 ± 0.002 $Å^{-1}$ and 0.002 ± 0.001 $Å^{-1}$ for Au-$[\mathbf{A_A(CoL_A)}_{n+1}\mathbf{FeL_A}]$ and Au-$[\mathbf{A_A(CoL_{L1})}_{n+1}\mathbf{FeL_{L1}}]$, respectively (Fig. 12d). These values are smaller than that of the iron complex wires, indicating the superior long-range electron transport ability of the $[Co(tpy)_2]^{3+}$ complex wires over that of $[Fe(tpy)_2]^{2+}$. The electron transport ability of bis(terpyridine)metal complex wires can therefore be regulated by the metal centre.

Four types of bis(terpyridine)iron(II) complex wires were prepared to study the redox-molecule-appended terminal ligand **T**: Au-$[\mathbf{A_H(FeL_{L1})}_n\mathbf{FeT_{Ru}}]$, Au-$[\mathbf{A_H(FeL_{L1})}_n\mathbf{FeT_{TAA}}]$, Au-$[\mathbf{A_H(FeL_{L1})}_n\mathbf{FeT_{Fc1}}]$, and Au-$[\mathbf{A_H(FeL_{L1})}_n\mathbf{FeT_{Fc2}}]$ (Fig. 12e). All terminal redox sites possessed formal potentials similar to one another. As with the surface-anchor ligand **A**, the β values converged to a narrow range (0.017–0.025 $Å^{-1}$), whereas k_0 was somewhat scattered. This effect is likely due to the difference in

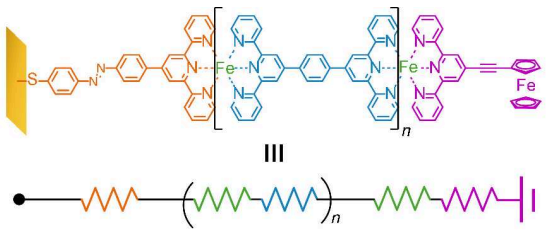

Fig. 11 Concept of a molecular circuit based on the bis(terpyridine)metal complex wire.

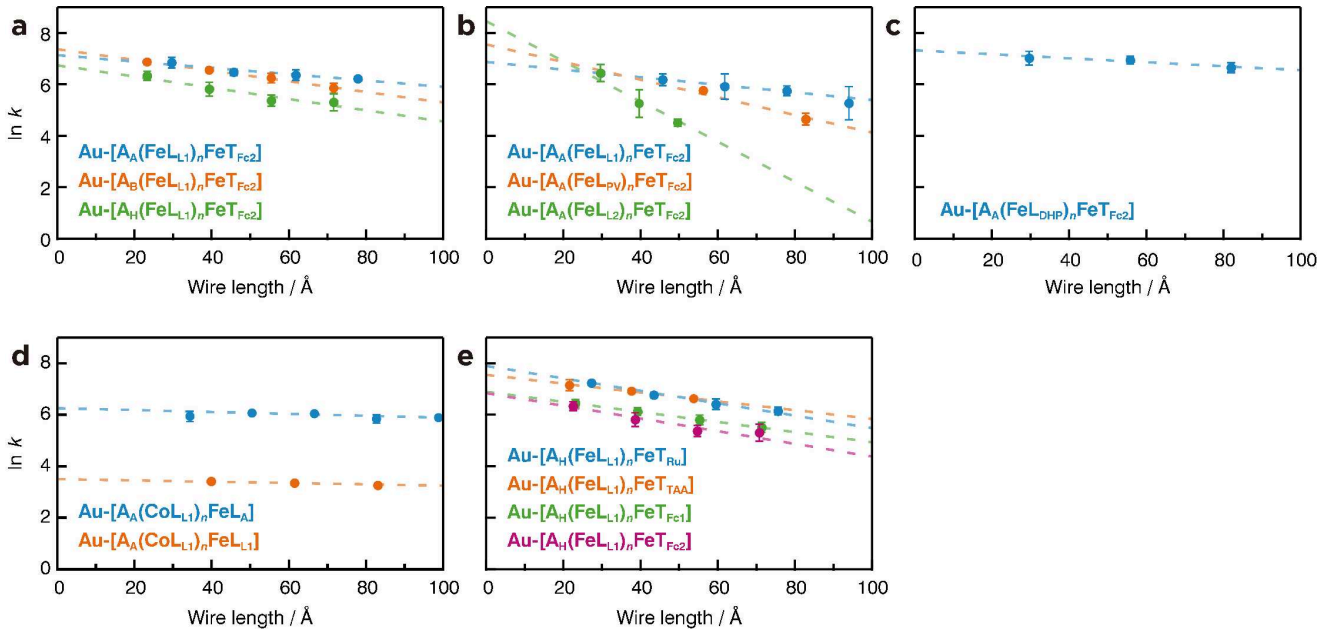

Fig. 12 ln*k*-*d* plots for the bis(terpyridine)metal complex wire. The dashed lines are obtained by means of the least squares. (a) Dependence on surface-anchor terpyridine ligand **A**, with data for Au-**[A$_A$(FeL$_{L1}$)$_n$FeT$_{Fc2}$]** (blue), Au-**[A$_B$(FeL$_{L1}$)$_n$FeT$_{Fc2}$]** (orange), and Au-**[A$_H$(FeL$_{L1}$)$_n$FeT$_{Fc2}$]** (green). (b) Dependence on bridging terpyridine ligand **L**, with data for Au-**[A$_A$(FeL$_{L1}$)$_n$FeT$_{Fc2}$]** (blue), Au-**[A$_A$(FeL$_{PV}$)$_n$FeT$_{Fc2}$]** (orange), and Au-**[A$_A$(FeL$_{L2}$)$_n$FeT$_{Fc2}$]** (green). (c) Smallest □ among **L** series with Au-**[A$_A$(FeL$_{DHP}$)$_n$FeT$_{Fc1}$]**. (d) Dependence on metal ions, with Au-**[A$_A$(CoL$_A$)$_{n+1}$]** (blue) and Au-**[A$_A$(CoL$_{L1}$)$_{n+1}$]** (orange). (e) Dependence on terminal ligand **T**, with Au-**[A$_H$(FeL$_{L1}$)$_n$FeT$_{Ru}$]** (blue), Au-**[A$_H$(FeL$_{L1}$)$_n$FeT$_{TAA}$]** (orange), Au-**[A$_H$(FeL$_{L1}$)$_n$FeT$_{Fc1}$]** (green), and Au-**[A$_H$(FeL$_{L1}$)$_n$FeT$_{Fc2}$]** (magenta). Adapted with permission from ref. 17c,d,h. Copyright 2009, 2013 Wiley-VCH Verlag GmbH&Co. KGaA, and 2010 American Chemical Society.

reorganization energy λ. Triarylamine and cyclometallated ruthenium complexes possess smaller λ and therefore exhibit greater electron transfer rates.

The PSCA technique revealed the excellent long-range electron transport ability of the linear bis(terpyridine)metal complex wires. The smallest values were 0.002 and 0.008 Å^{-1} for the cobalt and iron wires, respectively, which are comparable with the smallest reported β values.[44,45] This type of PCSA experiment is simple and easy to conduct, but its results are often associated with the electrical conductivity of the molecular wire using elaborate and difficult molecular junction techniques.[65–68] Our results were well aligned with a shallow distance dependence of the electrical conductivity of bis(terpyridine)metal complex wires.[68] The long-range electron transport ability can be controlled by designing the wire's constituents, and this methodology is useful when constructing molecular-scale electronic devices.

2.4 Elucidation of the long–range electron transport phenomenon

Understanding how electrons travel through "branched" molecular wires in the long-range electron transport scheme is essential in developing molecular parallel circuits[69] and splitters.[70] However, branched molecular wires are rarely precisely fabricated,[71,72] and such investigations therefore have yet to be addressed. As demonstrated in Fig. 3b, c, dendritic wires can be fabricated for the bis(terpyridine)metal complex wire system in addition to common linear wires. A characteristic electron transport phenomenon was observed in the branched oligomer wire furnished with terminal ferrocene units (Au-**[A$_H$(FeL$_{T1}$)$_n$FeT$_{Fc2}$]**, Fig. 3c), establishing an effective kinetic simulation model based on intra-wire sequential electron hopping.

Fig. 13a-c displays the PSCAs for the oxidation and reduction of the terminal ferrocene in Au-**[A$_H$(FeL$_{T1}$)$_n$FeT$_{Fc2}$]** (n = 1–3). The PSCA profiles (i_{exp}–t plot) feature asymmetric electron transport. Deviation from normal exponential decay was more substantial in the oxidation process, which contained an unusual plateau–like region. The asymmetry in the electron transport became more pronounced as n increased. This series of current decay profiles is completely different from those of previously reported linear molecular wire systems furnished with redox-active termini. A simple, effective electron transport

Table 1. k_0 and β values for the bis(terpyridine)metal complex wire

	wire	β	k_0 (s^{-1})
Anchor ligand **A**	Au-**[A$_A$(FeL$_{L1}$)$_n$FeT$_{Fc2}$]**	0.014±0.004	1.3×10^3
	Au-**[A$_B$(FeL$_{L1}$)$_n$FeT$_{Fc2}$]**	0.020±0.004	1.6×10^3
	Au-**[A$_H$(FeL$_{L1}$)$_n$FeT$_{Fc2}$]**	0.024±0.007	8.5×10^2
Bridging ligand **L**	Au-**[A$_A$(FeL$_{DHP}$)$_n$FeT$_{Fc1}$]**	0.008±0.006	1.5×10^3
	Au-**[A$_A$(FeL$_{L1}$)$_n$FeT$_{Fc2}$]**	0.015±0.007	9.6×10^2
	Au-**[A$_A$(FeL$_{PV}$)$_n$FeT$_{Fc2}$]**	0.031±0.008	2.0×10^3
	Au-**[A$_A$(FeL$_{L2}$)$_n$FeT$_{Fc2}$]**	0.070±0.020	4.7×10^3
Metal ion	Au-**[A$_A$(CoL$_A$)$_{n+1}$FeL$_A$]**	0.002±0.001	3.3×10
	Au-**[A$_A$(CoL$_{L1}$)$_{n+1}$FeL$_{L1}$]**	0.004±0.002	5.3×10^2
Terminal ligand **T**	Au-**[A$_H$(FeL$_{L1}$)$_n$FeT$_{TAA}$]**	0.017±0.005	1.9×10^3
	Au-**[A$_H$(FeL$_{L1}$)$_n$FeT$_{Ru}$]**	0.024±0.003	2.7×10^3
	Au-**[A$_H$(FeL$_{L1}$)$_n$FeT$_{Fc1}$]**	0.025±0.007	9.3×10^2
	Au-**[A$_H$(FeL$_{L1}$)$_n$FeT$_{Fc2}$]**	0.020±0.004	9.9×10^2

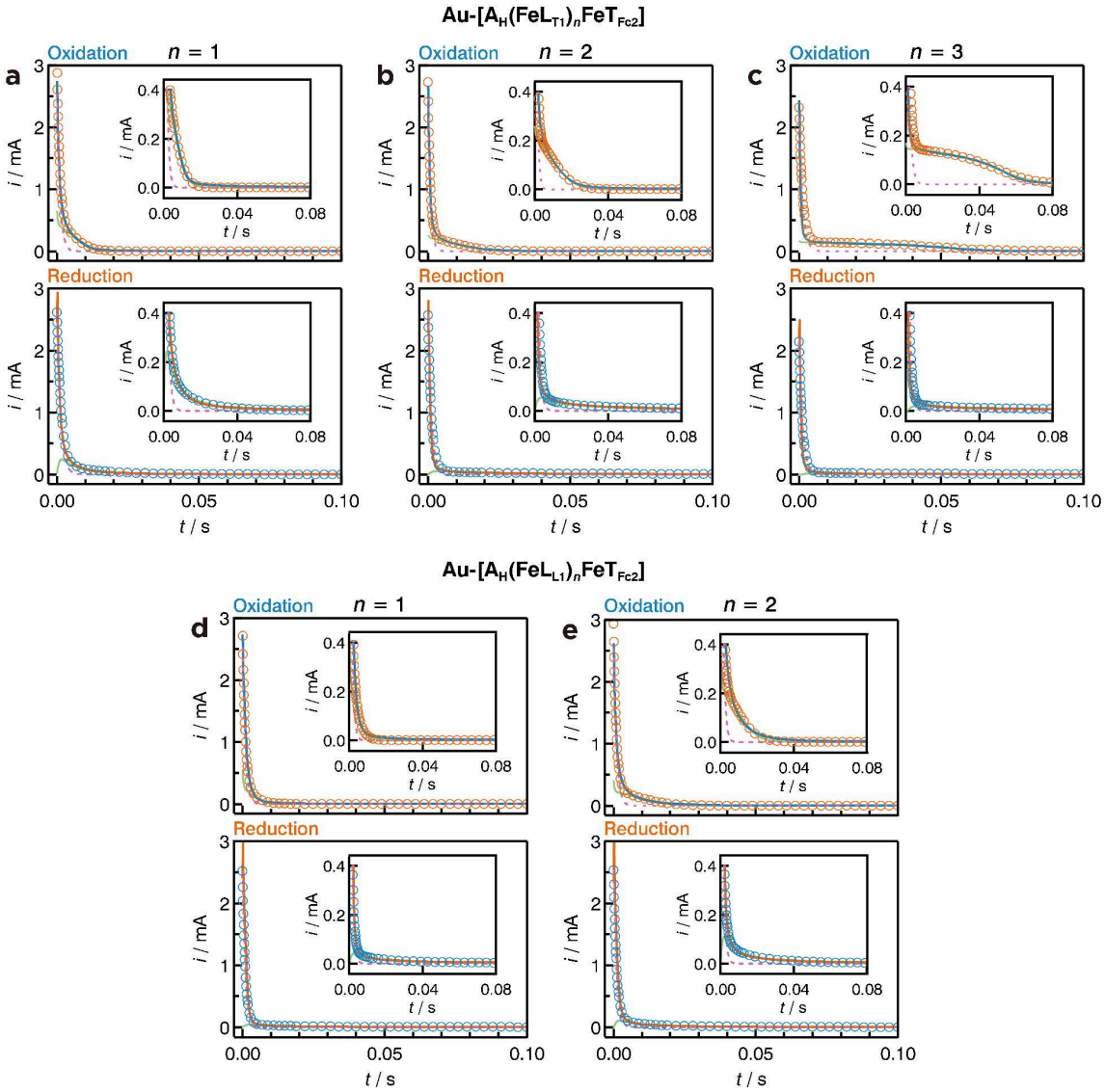

Fig. 13 Long-range electron transport through Fe(tpy)$_2$ branched and linear oligomer wires. Representative experimental (i_{exp}–t) and simulated (i_{sim}–t) plots for: (a) Au-**[A$_H$(FeL$_{T1}$)FeT$_{Fc2}$]**, (b) Au-**[A$_H$(FeL$_{T1}$)$_2$FeT$_{Fc2}$]**, (c) Au-**[A$_H$(FeL$_{T1}$)$_3$FeT$_{Fc2}$]**, (d) Au-**[A$_H$(FeL$_{L1}$)FeT$_{Fc2}$]**, (e) Au-**[A$_H$(FeL$_{L1}$)$_2$FeT$_{Fc2}$]**. Legend. Blue solid line: i_{exp} for oxidation with an overpotential of +0.35 V for the terminal ferrocene moiety; orange solid line: i_{exp} for reduction with –0.35 V; magenta dashed line: electric double layer charging current i_{DL}; green solid line: faradaic current i_F; orange circles; i_{sim} for the oxidation; blue circles: i_{sim} for the reduction. Used parameters: (a) for oxidation: k_1 = 340 s^{-1}, k_{-1} = 4.0 × 10^3 s^{-1}, $k_{\pm2}$ = 1.77 × 10^4 s^{-1}, k_3 = 4.7 × 10^3 s^{-1}, k_{-3} = 18 s^{-1}, C_{dl} = 4.0 μF; for reduction: k_1 = 0 s^{-1}, k_{-1} = 1.8 × 10^3 s^{-1}, $k_{\pm2}$ = 1.77 × 10^4 s^{-1}, k_3 = 4.7 × 10^3 s^{-1}, k_{-3} = 240 s^{-1}, C_{dl} = 5.0 μF. (b) for oxidation: k_1 = 310 s^{-1}, k_{-1} = 3.2 × 10^3 s^{-1}, $k_{\pm2}$ = 1.73 × 10^4 s^{-1}, k_3 = 5.2 × 10^3 s^{-1}, k_{-3} = 130 s^{-1}, C_{dl} = 3.1 μF; for reduction: k_1 = 0.002 s^{-1}, k_{-1} = 4.4 × 10^3 s^{-1}, $k_{\pm2}$ = 1.73 × 10^4 s^{-1}, k_3 = 5.2 × 10^3 s^{-1}, k_{-3} = 31 s^{-1}, C_{dl} = 4.7 μF. (c) for oxidation: k_1 = 210 s^{-1}, k_{-1} = 5.0 × 10^3 s^{-1}, $k_{\pm2}$ = 1.79 × 10^4 s^{-1}, k_3 = 5.2 × 10^3 s^{-1}, k_{-3} = 17 s^{-1}, C_{dl} = 4.0 μF; for reduction: k_1 = 10 s^{-1}, k_{-1} = 5.0 × 10^3 s^{-1}, $k_{\pm2}$ = 1.79 × 10^4 s^{-1}, k_3 = 5.2 × 10^3 s^{-1}, k_{-3} = 5 s^{-1}, C_{dl} = 4.0 μF. (d) for oxidation: k_1 = 3.2 × 10^2 s^{-1}, k_{-1} = 4.0 × 10^3 s^{-1}, $k_{\pm2}$ = 1.7 × 10^4 s^{-1}, k_3 = 5.6 × 10^3 s^{-1}, k_{-3} = 31 s^{-1}, C_{dl} = 3.7 μF; for reduction: k_1 = 0 s^{-1}, k_{-1} = 1.3 × 10^3 s^{-1}, $k_{\pm2}$ = 1.7 × 10^4 s^{-1}, k_3 = 5.6 × 10^3 s^{-1}, k_{-3} = 63 s^{-1}, C_{dl} = 3.7 μF. (e) for oxidation: k_1 = 2.1 × 10^2 s^{-1}, k_{-1} = 5.0 × 10^3 s^{-1}, $k_{\pm2}$ = 1.6 × 10^4 s^{-1}, k_3 = 5.5 × 10^3 s^{-1}, k_{-3} = 14 s^{-1}, C_{dl} = 4.0 μF; for reduction: k_1 = 3.3 s^{-1}, k_{-1} = 1.8 × 10^3 s^{-1}, $k_{\pm2}$ = 1.6 × 10^4 s^{-1}, k_3 = 5.5 × 10^3 s^{-1}, k_{-3} = 1.3 × 10^2 s^{-1}, C_{dl} = 4.0 μF. Adapted with permission from ref. 17k. Copyright 2015 American Chemical Society.

numerical model was used to elucidate the unique electron transport in the branched wire. Fig. 14a-c illustrates the electron transfer model, which is more or less associated with the redox conduction model in Fig. 9. In this scheme, an electron sent from the gold electrode to the terminal ferrocenium, or from the terminal ferrocene to the gold electrode, is allowed to hop between the neighbouring redox-active sites (i.e., terminal ferrocene and Fe(tpy)$_2$ units) and the gold electrode in an intra-wire manner. The redox-active site can occupy two states, electron-filled (ferrocene^0 and [Fe(tpy)$_2$]$^{2+}$) and electron-deficient (ferrocene$^+$ and [Fe(tpy)$_2$]$^{3+}$). The gold electrode functions as an electron reservoir, accepting or providing infinite numbers of electrons. The hopping process consists of three steps. The first is between the gold electrode and first-

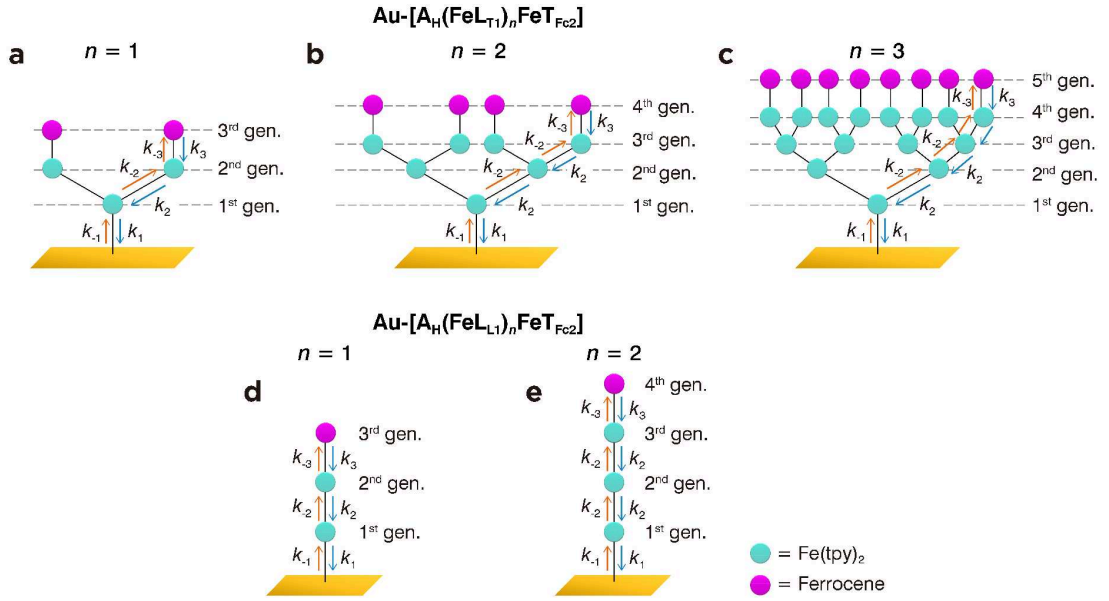

Fig. 14 Long-range electron transport models for(a) Au-$[A_H(FeL_{T1})FeT_{Fc2}]$, (b) Au-$[A_H(FeL_{T1})_2FeT_{Fc2}]$, (c) Au-$[A_H(FeL_{T1})_3FeT_{Fc2}]$, (d) Au-$[A_H(FeL_{L1})FeT_{Fc2}]$, (e) Au-$[A_H(FeL_{L1})_2FeT_{Fc2}]$. Magenta and turquoise circles stand for the $Fe(tpy)_2$ and terminal ferrocene units, respectively. Adapted with permission from ref. 17k. Copyright 2015 American Chemical Society.

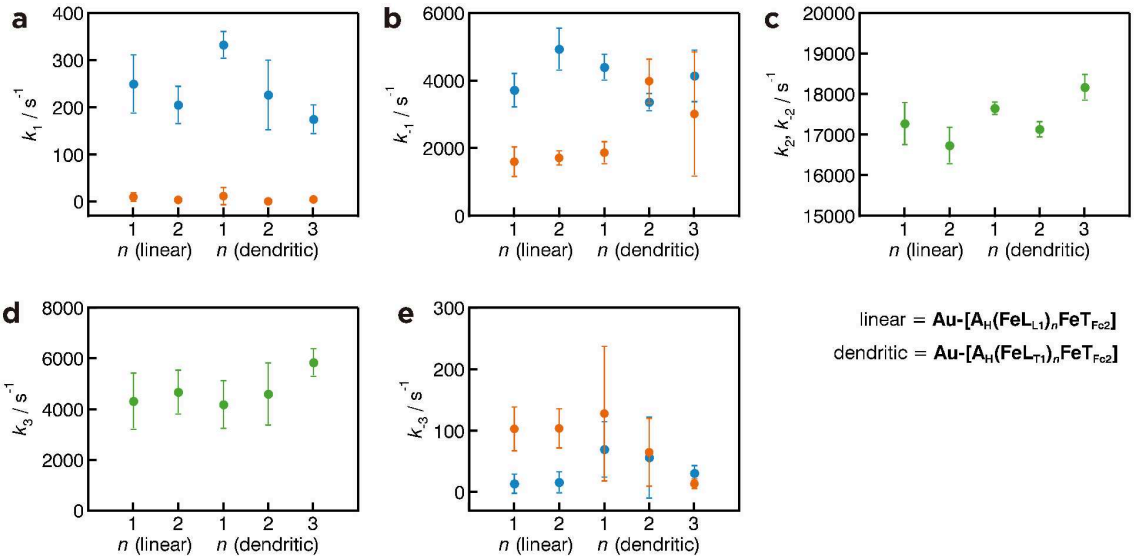

Fig. 15 Average electron transfer rate constants k_m (m= ±1, ±2, ±3) extracted from the simulation for branched Au-$[A_H(FeL_{T1})_nFeT_{Fc2}]$ (n = 1–3) and linear Au-$[A_H(FeL_{L1})_nFeT_{Fc2}]$ (n = 1, 2). Blue and red plots exhibit the rate constants for oxidation and reduction, and green ones for constrained parameters. (a) k_1, (b) k_{-1}, (c) k_2 and k_{-2}, (d) k_3, (e) k_{-3}. Adapted with permission from ref. 17k. Copyright 2015 American Chemical Society.

generation $Fe(tpy)_2$ unit (see Fig. 14a-c for a definition of the generation). The rate constants for electron injection from the $Fe(tpy)_2$ unit to the electrode and vice versa are represented as k_1 and k_{-1}, respectively. Second, electron exchange between adjacent $Fe(tpy)_2$ units features second-order electron self-exchange rate constants k_2 and k_{-2}. Third, electron hopping between the terminal ferrocene and neighbouring $Fe(tpy)_2$ unit has second-order rate constants of k_3 and k_{-3}. A set of kinetic equations for Au-$[A_H(FeL_{T1})_nFeT_{Fc2}]$ is expressed as follows:

$$dP_1/dt = 2[k_2P_2(1-P_1) - k_{-2}P_1(1-P_2)] - k_1P_1 + k_{-1}(1-P_1) \quad (8a)$$

$$dP_k/dt = 2[k_2P_{k+1}(1-P_k) - k_{-2}P_k(1-P_{k+1})] - k_2P_k(1-P_{k-1}) + k_{-2}P_{k-1}(1-P_k) \quad (k = 2, 3,\ldots, n) \tag{8b}$$

$$dP_{n+1}/dt = k_3P_{n+2}(1-P_{n+1}) - k_{-3}P_{n+1}(1-P_{n+2}) - k_2P_{n+1}(1-P_n) + k_{-2}P_n(1-P_{n+1}) \tag{8c}$$

$$dP_{n+2}/dt = -k_3P_{n+2}(1-P_{n+1}) + k_{-3}P_{n+1}(1-P_{n+2}) \tag{8d}$$

The faradaic current of the terminal ferrocene, i_F, is expressed as follows:

$$i_F = FA\Gamma[k_1P_1 - k_{-1}(1-P_1)] \tag{9}$$

The simulated total current i_{sim} is shown as eq. (6). Identical to the redox conduction in Section 2.2, the numerical simulation corresponds to reproducing i_{exp} with i_{sim} and varying the k_m (m = ±1, ±2, ±3) values. The resultant i_{sim} (as orange or blue circles) was consistent with the experimental current–time profile (Fig. 13a–c). The terms i_{DL} (magenta dashed line) and i_F (green solid line) highlight how i_F plays a chief role in the characteristic plateau region of the oxidation process.

The linear wire Au-$\mathbf{[A_H(FeL_{L1})_nFeT_{Fc2}]}$ (n = 1 and 2; Fig. 13d,e) was reproduced to verify the electron transport model and simulation thereof. Provided that the set of electron-hopping processes is the same as for the branched wire (i.e., Fig. 14d,e), the kinetic equations for the linear wire are represented as follows:

$$dP_1/dt = k_2P_2(1-P_1) - k_{-2}P_1(1-P_2) - k_1P_1 + k_{-1}(1-P_1) \tag{10a}$$

$$dP_k/dt = k_2P_{k+1}(1-P_k) - k_{-2}P_k(1-P_{k+1}) - k_2P_k(1-P_{k-1}) + k_{-2}P_{k-1}(1-P_k) \quad (k = 2, 3,\ldots, n) \tag{10b}$$

$$dP_{n+1}/dt = k_3P_{n+2}(1-P_{n+1}) - k_{-3}P_{n+1}(1-P_{n+2}) - k_2P_{n+1}(1-P_n) + k_{-2}P_n(1-P_{n+1}) \tag{10c}$$

$$dP_{n+2}/dt = -k_3P_{n+2}(1-P_{n+1}) + k_{-3}P_{n+1}(1-P_{n+2}) \tag{10d}$$

The faradaic current i_F and simulated total current i_{sim} are obtained from equations (9) and (6), respectively. The resultant i_{sim}–t plots are overlain on the i_{exp}–t plots (Fig. 13d, e) and again are consistent.

Fig. 15 assembles the average electron transfer rate constants k_m (m = ±1, ±2, ±3) obtained from the simulation for branched Au-$\mathbf{[A_H(FeL_{T1})_nFeT_{Fc2}]}$ (n = 1–3) and linear Au-$\mathbf{[A_H(FeL_{L1})_nFeT_{Fc2}]}$ (n = 1, 2) using three independent samples. Each parameter was confined within a certain range, including its standard deviation, in both branched and linear wires, which is reasonable because the two wire systems contain the same metal ion (Fe^{2+}), anchor (**A**) and terminal (**T**) terpyridine ligands, as well as similar types of bridging terpyridine ligand (**L**).

Electron transport between the terminal ferrocene unit and gold electrode through the branched bis(terpyridine)iron(II) complex wire was investigated by PSCA, which revealed unusual asymmetric and non-exponential faradaic current decays. To elucidate this phenomenon, an electron transport mechanism based on intra-wire electron hopping between two adjacent redox active sites was established. Numerical simulation thereof reproduced the pattern of electron transport that characterized the branched wire. The same type of intra-wire electron hopping mechanism and simulation may also account for the electron-transport phenomenon in the linear bis(terpyridine)iron(II) complex wire. Simulated electron-hopping rate constants k_m (m = ±1, ±2, ±3) converged to similar values in the dendritic and linear wires, validating the electron transport mechanism. For the first time, the electron transport mechanism in a branched molecular wire system has been clarified, a milestone in the development of molecule-based circuits.

3. Fabrication and application of an ultra-long metal complex wire network

The construction of ultra-long linear metal complex wires is significant due to their resulting unique properties and ease of synthesis and modification.[73] Metal complex wires can be readily prepared under moderate coordination reaction conditions by mixing bridging ligands and metallic sources. By simply modifying the bridging ligands or changing the metal species or their valences, the structures and properties of such complex wires can be drastically altered. In comparison, most long linear materials with carbon backbones, such as carbon nanotubes[74] and conducting polymers,[75] are more difficult to modify, often requiring extra post-production treatments or longer synthetic procedures. This difficulty can reduce their stability or restrict precise changes in physical properties to achieve higher functionality.

Moreover, because metal complex wires can be fabricated under mild conditions, many methods can generate well-ordered superstructures, such as template assisting,[76] self-assembly,[77] and interfacial synthesis.[78] The uniform and well-

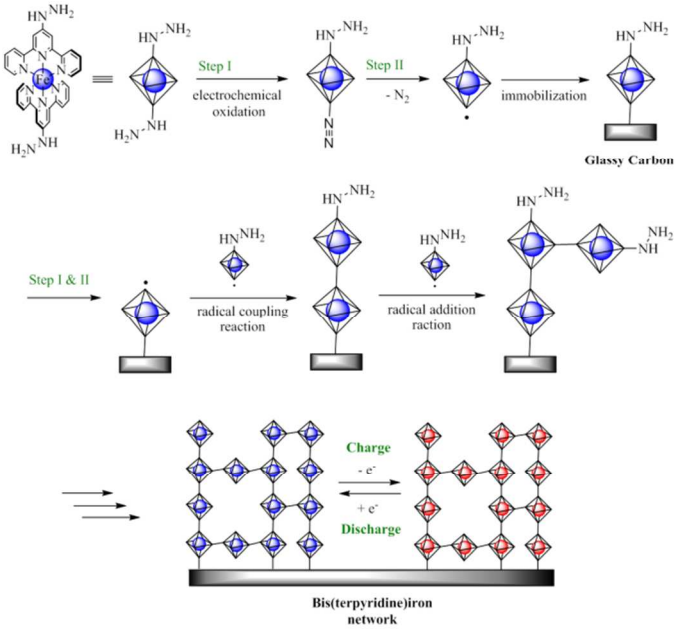

Fig. 16 Fabrication process for bis(terpyridine)Fe(II) metal complex network and its charging/discharging. Blue sphere: Fe(II); red sphere: Fe(III). Adapted with permission from ref. 18. Copyright 2013 Royal Chemical Society.

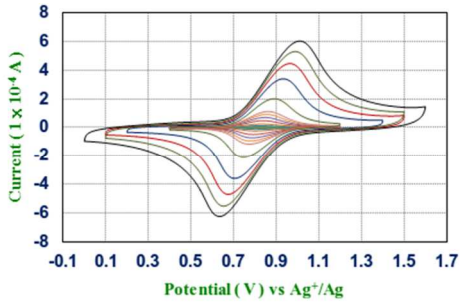

Fig. 17 Cyclic voltammograms of the bis(terpyridine)iron polymer network at various scan rates (0.01, 0.05, 0.10, 0.20, 0.40, 0.60, 0.80, 1.00, 2.00, 4.00, 6.00, 8.00 and 10.00 V s^{-1}) in 0.1 M Bu_4NClO_4–acetonitrile. The peak current increases with a greater scan rate. Adapted with permission from ref. 18. Copyright 2013 Royal Chemical Society.

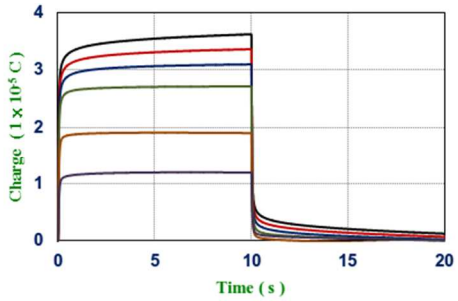

Fig. 18 Chronocoulomograms measured in 0.1 M Bu_4NClO_4–acetonitrile. Potential step: 0.10 V (from 0.75 to 0.85 V vs Ag^+/Ag); 0.20 V (from 0.70 to 0.90 V); 0.40 V (from 0.60 to 1.00 V), 0.60 V (from 0.50 to 1.10 V); 0.80 V (from 0.40 to 1.20 V); 1.00 V (from 0.30 to 1.30 V). Adapted with permission from ref. 18. Copyright 2013 Royal Chemical Society.

ordered wire structures (i.e., primary structure) are essential to achieving synergetic performances, excluding random behaviour. Most carbon-backboned long linear materials are synthesized under harsh and uncontrolled conditions (i.e., chemical vapour deposition reactions under high temperature[79] or polymerization reactions catalysed by free radicals,[73] cations or anions).[80] These methods create long wires with various lengths and random chemical structures. Additionally, the inter-wire structures (i.e., secondary structure) cannot be adequately controlled, resulting in randomly aggregated materials. Therefore, long linear π-conjugated metal complex wires are promising materials for future applications.

3.1 Electrochemical synthesis of a bis(terpyridine)iron(II) complex network

Bis(terpyridine)iron(II) complex wires were tethered to each other by covalent bonds to form a network structure (Fig. 16).[19] Similar to the linear wires, this network featured rapid electron transport, giving rise to distant redox conduction with respect to the Fe^{3+}/Fe^{2+} couple. The network densely accumulated the metal complex wires but still preserved a porous structure, which ensured a pathway for the electrolyte. These properties are all critical in an ideal electric storage material.

An electrochemically induced free radical coupling reaction constructed the iron bis(terpyridine) network complex (Fig. 16). The free radical monomer was generated from a stable precursor, bis(4'-hyrazinylterpyridine)Fe(II) complex. Initially, the hydrazine group was converted to a diazonium group by electrochemical oxidation assisted by superoxide. Molecular nitrogen was then eliminated, producing an aryl free radical. This product undergoes immobilization onto the glassy carbon electrode,[81] which then serves as a scaffold. The vertical growth of the molecular wire relies on free radical coupling,[82] whereas free radical addition forms the horizontal network.[83] In both cases, a covalent carbon-carbon bond is formed. A representative AFM image revealed many particles on the HOPG electrode. The average height of the particles was ca. 60 nm, corresponding to 55 units of the $Fe(tpy)_2$ complex.

Electrochemical measurements evaluated the charge storage ability of the complex network. Cyclic voltammetry disclosed a stable and reversible redox wave of the Fe(III)/Fe(II) couple at 0.78 V versus Ag^+/Ag (Fig. 17). The capacity of the complex network derived from the Fe(III)/Fe(II) redox couple decreased slightly as the scan rate increased. Additionally, the peak separation of the Fe(III)/Fe(II) redox couple was rather small, even at large scan rates. This series of results indicates that the intra-wire redox conduction and accompanying counter-anion transfer is smooth enough to realize a rapid charge/discharge. The charge/discharge behaviour was further investigated by chronocoulometry (Fig. 18) and chronoamperometry. The specific capacity of this material reached 55.5 mAh g^{-1} at a potential step of 1.0 V. Its discharge rate was 280 A g^{-1}, corresponding to a capacity retention of 80%. This material could be charged and discharged to 95% in 0.35 s and 0.62 s, respectively. This networked material also featured extremely high stability. It endured 3000 charging/discharging cycles with a capacity loss of only 5%.

4. Conclusions

In this review, we discussed electron conduction in bis(terpyridine)metal complex molecular wires. Their precise fabrication was realized through the bottom-up method using a stepwise coordination reaction on the electrode surface. This method provided both linear and branched structures of π-conjugated bis(terpyridine)metal complex oligomers. A series of electrochemical analyses on the electron transfer kinetics revealed characteristic intra-wire redox conduction and superior long-range electron transport ability. The electron transfer kinetics were analysed systematically and quantitatively, yielding comprehensive knowledge on how each component of the metal complex wire influences electron transport. In addition, an electropolymerization method afforded a network structure based on ultra-long π-conjugated bis(terpyridine)iron(II) complex polymer wires. The modified electrode exhibited persistent and rapid charge/discharge behaviour. One of the remaining challenges lies in applications to single-wire electronics by exploiting break junction and STM techniques.[84] A fundamental and comprehensive understanding of electron transfer and transport phenomena in π-conjugated redox-active molecular wires will contribute to the design and realization of molecular electronic circuits and to the development of high-end electrochemical and bioelectrochemical devices driven under wet conditions, such as sensors and energy storage systems.

Acknowledgements

The authors acknowledge Grants-in-Aid from MEXT of Japan (Nos. 21108002, 24750054, 25107510, 26110505, 26220801, 26248017, 26708005, 26107510, 26620039, areas 2107 [Coordination Programming], 2406 [All Nippon Artificial Photosynthesis Project for Living Earth], 2506 [Science of Atomic Layers], 2509 [Molecular Architectonics]), and JSPS fellowship for young scientists. R.S. is grateful to The Japan

Prize Foundation, Iketani Science and Technology Foundation, The Murata Science Foundation, Tokuyama Science Foundation, Ogasawara Foundation for the Promotion of Science & Engineering, The Kao Foundation for Arts and Sciences, The Asahi Glass Foundation, The Noguchi Institute, Japan Association for Chemical Innovation, The MIKIYA Science and Technology Foundation, Yazaki Memorial Foundation for Science and Technology, Shorai Foundation for Science and Technology, The Kurata Memorial Hitachi Science and Technology Foundation, and Kumagai Foundation for Science and Technology for financial supports. K.-H.W appreciate Interchange Association, Japan for a scholarship. R.M. and H.M. acknowledge JSPS fellowship for young scientists.

Notes and references

Department of Chemistry, Graduate School of Science, The University of Tokyo, 7-3-1, Hongo, Bunkyo-ku, Tokyo 113-0033, Japan

1 (a) H. Nishihara, *Chem. Lett.*, 2014, **43**, 388–395. (b) Y. Yin, D. Talapin *Chem. Soc. Rev.,* 2013, **42**, 2484-2498. (c) E. Ruiz-Hitzky, P. Aranda, M. Darder, M. Ogawa, *Chem. Soc. Rev.*, 2011, **40**, 801-828. (d) S. A. Claridge, W.-S. Liao, J. C. Thomas, Y. Zhao, H. H. Cao, S. Cheunkar, A. C. Serino, A. M. Andrews, P. S. Weiss, *Chem. Soc. Rev.*, 2013, **42**, 2725-2745. (e) A. Mehdi, C. Reye, R. Corriu, *Chem. Soc. Rev.*, 2011, **40**, 563-574.

2. (a) W. Tong, X. Song, C. Gao, *Chem. Soc. Rev.*, 2012, **41**, 6103-6124. (b) J. Borges, J. F. Mano, *Chem. Rev.*, 2014, **114**, 8883-8942. (c) Y. Li, X. Wang, J. Sun, *Chem. Soc. Rev.*, 2012, **41**, 5998-6009. (d) Y. Xiang, S. Lua, S. P. Jiang, *Chem. Soc. Rev.*, 2012, **41**, 7291-7321.

3. (a) P. K. B. Palomaki, P. H., Dinolfo, *Langmuir,* 2010, **26**, 9677-9685. (b) A. P. Upadhyay, D. K. Behara, G. P. Sharma, A. Bajpai, N. Sharac, R. Ragan, R. G. S. Pala, S. Sivakumar, *ACS Appl. Mater. Interface,* 2013, **5**, 9554-9562. c) L. Luo, C. D. Frisbie, *J. Am. Chem. Soc.,* 2010, **132**, 8854-8855.

4. (a) S. H. Choi, B. Kim, C. D. Frisbie, *Science* 2008, **320**, 1482-1486. (b) S. H. Choi, C. Risko, M. C. R. Delgado, B. Kim, J.-L. Brédas, C. D. Frisbie, *J. Am. Chem. Soc.* 2010, **132**, 4358-4368.

5. (a) J. Liu, M. Chen, D.-J. Qian, *Colloid. Surface. A,* 2013, **436**, 953-960. (b) S. W. Lee, B.-S. Kim, S. Chen, Y. Shao-Horn, P. T. Hammond, *J. Am. Chem. Soc.,* 2009, **131**, 671-679. (c) G. Decher, *Science,* 1997, **29**, 1232-1237.

6. (a) A. Shida, H. Sugimura, M. Futsuhara, O. Takai, *Surf. Coat. Tech.,* 2003, **169-170**, 686-690. (b) H. Sugimura, H. Yonezawa, S. Asai, Q.-W. Sun, T. Ichii, K.-H. Lee, K. Murase, K. Noda, K. Matsushige, *Colloid Surface A,* 2008, **321**, 249-253. (c) Y. Chaikin, H. Leader, R. Popovitz-Biro, A. Vaskevich, I. Rubinstein, *Langmuir,* 2011, **27**, 1298-1307. (d) Wanunu, M. R. Popovitz-Biro, H. Cohen, A. Vaskevich, I. Rubinstein, *J. Am. Chem. Soc.* 2005, **127**, 9207-9215. (e) H. Wanunu, A. Vaskevich, S. R. Cohen, H. Cohen, R. Arad-Yellin, A. Shanzer, I. Rubinstein, *J. Am. Chem. Soc.* 2005, **127**, 17877-17887. (f) L. Oo, F. Kitamura, *J. Electroanal. Chem.* 2008, **619-620**, 187-192.

7. (a) L. Motiei, M. Feller, G. Evmenenko, P. Dutta, M. E. van der Boom, *Chem. Sci.,* 2012, **3**, 66-71. (b) P. C. Mondal, J. Y. Lakshmanan, H. Hamoudi, M. Zharnikov, P. C. Gupta, *J. Phys. Chem. C,* 2011, **115**, 16398-16404. (c) Y.-Q. Cai, X.-B. Ren, H.-L. Wang, H.-X. Huang, M. Chen, D.-J. Qian, *Synthetic Met.,* 2012, **162**, 1871-1878. (d) H.-T. Chen, B. Liu, H.-T. Wang, Z.-D. Xiao, M. Chen, D.-J. Qian, *Mat. Sci. Eng. C,* 2007, **27**, 639-645. (e) S. Gao, Y. Huang, M. Cao, T.-f. Liu, R. Cao, *J. Mater. Chem.,* 2011, **21**, 16467-16472. (f) M. Altman, A. D. Shukla, T. Zubkov, G. Evmenenko, P. Dutta, M. E. van der Boom, *J. Am. Chem. Soc.,* 2006, **128**, 7374-7382. (g) X.-B. Ren, M. Chen, D.-J. Qian, *Langmuir,* 2012, **28**, 7711-7719. (h) P. C. Mondal, M. Chhatwal, Y. Lakshmanan, L. Zharnikov, M. Jeyachandran, *J. Phys. Chem. C,* 2014, **118**, 9578-9587. (i) Y. Tang, M. Chen, D.-J. Qian, L. Zhang, M. Liu, *Colloid Surface A,* 2014, **457**, 41-48.

8. (a) O. Shekhah, H. Wang, T. Strunskus, P. Cyganik, D. Zacher, R. Fischer, C. Wöll, *Langmuir,* 2007, **23**,7440-7442. (b) J. Liu, M. Chen. D.-J. Qian, *Langmuir,* 2012, **28**, 9496-9505. (c) K. Kanaizuka, R. Haruki, O. Sakata, M. Yoshimoto, Y. Akita, H. Kitagawa, *J. Am. Chem. Soc.,* 2008, **130**, 15778-15779. (d) I. Schrader, L. Witting, K. Richter, H. Vieker, A. Beyer, A. Gölzhäuser, A. Hartwig, P. Swiderek. *Langmuir,* 2014, **30**, 11945-11954.

9. (a) W. Zhao, B. Tong, J. Shi, Y. Pan, J. Shen, J. Zhi, W. K. Chan, Y. Dong, *Langmuir,* 2010, **26**, 16084-16089. (b) B. Tong, H. Yang, W. Xiong, F. Xie, J. Shi, J. Zhi, W. K. Chan, Y. Dong, *J. Phys. Chem. B,* 2013, **117**, 5338-5344.

10. (a) M. Abe, T. Michi, A. Sato, T. Kondo, W. Zhou, S. Ye, K. Uosaki, Y. Sasaki, *Angew. Chem. Int. Ed.,* 2003, 42, 2912-2915. (b) W. Zhao, B. Tong, Y. Pan, J. Shen, J. Zhi, J. Shi, Y. Dong, *Langmuir,* 2009, **25**, 11796-11801.

11. (a) M. Altman, O. V. Zenkina, T. Ichiki, M. A. Iron, G. Evmenenko, P. Dutta, M. E. van der Boom, *Chem. Mater.,* 2009, **21**, 4676-4684. (b) K. S. Lokesh, S. Chardon-Noblat, F. Lafolet, Y. Traoré, C. Gondran, P. Guionneau, L. Guérente, P. Labbé, A. Deronzier, J.-F. Létard, *Langmuir,* 2012, **28**, 11779-11789.

12. P. F. Driscoll, Jr., E. F. Douglass M. Phewluangdee, E. R. Soto, C. G. F. Cooper, J. C. MacDonald, C. R. Lambert, W. G. McGimpsey, *Langmuir,* 2008, **24**, 5140-5145.

13. Y. Tong, B. Pan, J. Shi, W. Zhao, J. Shen, J. Zhi, Y. Dong, *J. Phys. Chem. C,* 2010, **114**, 8040-8047.

14. F. B. Abdelrazzaq, R. C. Kwong, M. E. Thompson, *J. Am. Chem. Soc.,* 2002, **124**, 4796-4803.

15. C. Lin, C. R. Kagan, *J. Am. Chem. Soc.,* 2003, **125**, 336-337.

16. G. de Ruiter, M. Lahav, H. Keisar, M. E. van der Boom, *Angew. Chem. Int. Ed.,* 2013, **52**, 704-709.

17. (a) K. Kanaizuka, M. Murata, Y. Nishimori, I. Mori, K. Nishino, H. Masuda and H. Nishihara, *Chem. Lett.*, 2005, **34**, 534-535. (b) Y. Nishimori, K. Kanaizuka, M. Murata and H. Nishihara, *Chem. Asian J.*, 2007, **2**, 367-376. (c) Y. Nishimori, K. Kanaizuka, T. Kurita, T. Nagatsu, Y. Segawa, F. Toshimitsu, S. Muratsugu, M. Utsuno, S. Kume, M. Murata and H. Nishihara, *Chem. Asian J.* 2009, **8**, 1361-1367. (d) T. Kurita, Y. Nishimori, F. Toshimitsu, S. Muratsugu, S. Kume and H. Nishihara, *J. Am. Chem. Soc.*, 2010, **132**, 4524-4525. (e) H. Maeda, R. Sakamoto, Y. Nishimori, J. Sendo, F. Toshimitsu, Y. Yamanoi and H. Nishihara, *Chem. Commun.* 2011, **47**, 8644-8646. (f) Y. Nishimori, H. Maeda, S. Katagiri, J. Sendo, M. Miyachi, R. Sakamoto, Y. Yamanoi and H. Nishihara, *Macromol. Symp.* **2012**, *317-318*, 276–2850. (g) R. Sakamoto, Y. Ohirabaru, R. Matsuoka, H. Maeda, S. Katagiri and H. Nishihara, *Chem. Commum.*, 2013, **49**, 7108-7110. (h) S. Katagiri, R. Sakamoto, H. Maeda, Y. Nishimori, T.

Kurita and H. Nishihara, *Chem. Eur. J.*, 2013, **19**, 5088-5096. (i) R. Sakamoto, S. Katagiri, H. Maeda and H. Nishihara, *Chem. Lett.*, 2013, **42**, 361-362. (j) H. Maeda, R. Sakamoto, H. Nishihara, *Chem. Eur. J.*, 2014, **20**, 2761. (k) R. Sakamoto, S. Katagiri, H. Maeda, Y. Nishimori, S. Miyashita and H. Nishihara, *J. Am. Chem. Soc.*, **2015**, 137, 734–741. (l) R. Sakamoto, S. Katagiri, H. Maeda and H. Nishihara, *Coord. Chem. Rev.*, 2013, **257**, 1493–1506. (m) H. Nishihara, K. Kanaizuka, Y. Nishimori and Y. Yamanoi, *Coord. Chem. Rev.*, 2007, **251**, 2674–2687.

18. K.-H. Wu, H. Maeda, T. Kambe, K. Hoshiko, E. J. H. Phua, R. Sakamoto and H. Nishihara, *Dalton Trans.*, 2013, **42**, 15877–15880.
19. (a) A. Ulman, *Chem. Rev.*, 1996**, 96**, 1533–1554 (b) J. C. Love, L. A. Estroff, J. K. Kriebel, R. G. Nuzzo and G. M. Whitesides, *Chem. Rev.*, 2005**, 105**, 1103–1169.
20. (a) M. Abe, T. Michi, A. Sato, T. Kondo, W. Zhou, S. Ye, K. Uosaki and Y. Sasaki, *Angew. Chem. Int. Ed.*, 2003, **42**, 2912-2915. (b) M. Maskus, H. D. Abruña, *Langmuir*, 1996, **12**, 4455-4462. (c) M. Haga, T. Takasugi, A. Tomie, M. Ishizuya, Y. Yamada, M. D. Hossain and M. Inoue, *Dalton Trans.*, 2003, 2069-2079.
21. (a) N. Tajimi, H. Sano, K. Murase, K. H. Lee and H. Sugimura, *Langmuir*, 2007, **23**, 3193-3198. (b) S. Ciampi, P. K. Eggers, G. L. Saux, M. James, J. B. Harper and J. J. Gooding, *Langmuir*, 2009, **25**, 2530-2539. (c) Y. Liu, S. Yamazaki, S. Yambe and Y. Nakato, *J. Mater. Chem.*, 2005, **15**, 4906-4913. (d) J. M. Buriak, *Chem. Commun.*, 1999, 1051-1060.
22. (a) Y. Yamanoi *J. Org. Chem.*, 2005, **70**, 9607-9609. (b) A. Lesbani, H. Kondo, Y. Yabusaki, M. Nakai, Y. Yamanoi, H. Nishihara *Chem. Eur. J.*, 2010, **16**, 13519-13527. (c) A. Lesbani, H. Kondo, J. Sato, Y. Yamanoi, H. Nishihara *Chem. Commun.*, 2010, **46**, 7784-7786.
23. (a) P. G. Pickup and R. W. Murray, *J. Am. Chem. Soc.*, 1983, **105**, 4510–4514. (b) P. G. Pickup, W. Kutner, C. R. Leidner and R. W. Murray, *J. Am. Chem. Soc.*, 1984, **106**, 1991–1998. (c) E. D. Chidsey and R. W. Murray, *J. Phys. Chem.*, 1986, **90**, 1479–1484. (d) G. Zotti, G. Schiavon, S.Zecchin, A. Berlin, G. Pagani and A. Canavesi, *Synth. Met.*, 1996, **76**, 255–258. (e) J. Hjelm, R. W.Handel, A. Hagfeldt, E. C. Constable, C. E. Housecroft and R. J. Forster, *Inorg. Chem.*, 2005, **44**, 1073–1081.
24 (a) H. Nishihara and K. Aramaki, *J. Chem. Soc. Chem. Commun.*, 1985, 709–710. (b) H. Nishihara and K. Aramaki, *Chem. Lett.*, 1986, 1063–1064. (c) H. Nishihara, M. Noguchi and K. Aramaki, *Inorg. Chem.*, 1987, **26**, 2862–2869. (d) K. Sakamoto, H. Nishihara and K. Aramaki, *J. Chem. Soc. Dalton Trans.*, 1992, 1877–1882.
25 (a) P. G. Pickup and R. W. Murray, *J. Electrochem. Soc.*, 1984, **131**, 833–839. (b) H. C. Hurrell, H. D. Abruña, *Inorg. Chem.*, 1990, **29**, 736–741. (c) S. S. Zhu and T. M. Swager, *J. Am.Chem. Soc.*, 1997, **119**, 12568–12577.
26 (a) H. J. Dahms, *J. Phys. Chem.*, 1968, **72**, 362–364. (b) I. Ruff and V. J. Friedrich, *J. Phys. Chem.*, 1972, **76**, 162–168.
27 D. N. Blauch and J.-M. Savéant, *J. Am. Chem. Soc.*, 1992, **114**, 3323–3332.
28 (a) R. P. Buck, *J. Phys. Chem.*, 1988, **92**, 4196–4200. (b) J.-M. Savéant, *J. Electroanal. Chem. Interfacial. Electrochem.*, 1987, **242**, 1–8. (c) J.-M. Savéant, *J. Electroanal. Chem. Interfacial. Electrochem.* 1988, **242**, 1–21. (d) J.-M. Savéant, *J. Phys. Chem.*, 1988, **92**, 1011–1013. (e) J.-M. Savéant, *J. Phys. Chem.*, 1988, **92**, 4526–4532.
29 (a) P. Daum, J. R. Lenhard, D. Rolison, R. W. Murray, *J. Am. Chem. Soc.,* 1980, **102**, 4649-4653. (b) K.-N. Kuo, R. W. Murray, *J. Electro- anal. Chem. Interfacial. Electrochem.,* 1982, **131**, 37-60. (c) P. Burgmayer, R. W. Murray, *J. Electroanal. Chem. Interfacial. Electrochem.,* 1982, **135**, 335-342. (d) S. Nakahama, R.W. Murray, *J. Electroanal. Chem. Interfacial. Electrochem.,* 1983, **158**, 303-322. (e) K. Sigehara, N. Oyama, F. C. Anson, *J. Am. Chem. Soc.,* 1981, **103**, 2552 ‑2558. (f) C. R. Martin, I. Rubinstein, A. J. Bard, *J. Am. Chem. Soc.,* 1982, **104**, 4817-4824. (g) H. S. White, J. Leddy, A. J. Bard, *J. Am. Chem. Soc.,* 1983, **105**, 4811-4817. (h) L. Roullier, E. Waldner, E. Laviron, *J. Electroanal. Chem. Interfacial. Electrochem.,* 1982, **139**, 199-202. (i) L. Roullier, E. Waldner, *J. Electroanal. Chem. Interfacial. Electrochem.,* 1985, **187**, 97-107. (j) J. G. Eaves, H. S. Munro, D. Parker, *Inorg. Chem.*, 1987, **26**, 644-650 (k) R. A. Saraceno, G. H. Riding, H. R. Allcock, A. G. Ewing, *J. Am. Chem. Soc.*, 1988, **110**, 7254-7255.
30 C. Joachim, J. K. Gimzewski, A. Aviram, *Nature*, 2000, **408**, 541-548.
31 J. Park, A. N. Pasupathy, J. I. Goldsmith, C. Chang, Y. Yaish, J. R. Petta, M. Rinkoski, J. P. Sethna, H. D. AbruCa, P. L. McEuen, D. C. Ralph, *Nature,* 2002, **417**, 722-725.
32. S. Welter, K. Brunner, J. W. Hofstraat, L. D. Cola, *Nature*, 2003, **421**, 54-57.
33. E. D. Chidsey, R. W. Murray, *Science*, 1986, **231**, 25-31.
34. M. S. Wrighton, *Science*, 1986, **231**, 32-37.
35. O. S. Wenger, B. S. Leigh, R. M. Villahermosa, H. B. Gray, J. R. Winkler, *Science*, 2005, **307**, 99-102.
36. A. J. Bard, L. R. Faulkner, *Electrochemical Methods: Fundamentals and Applications*, 2nd ed., Wiley, New York, 2001.
37. C. E. D. Chidsey, *Science*, 1991, **251**, 919-922.
38. H. O. Finklea, D. D. E. Hanshew, *J. Am. Chem. Soc.*, 1992, **114**, 3173-3181.
39. M. T. Carter, G. K. Rowe, J. N. Richardson, L. M. Tender, R. H. Terrill, R.W. Murray, *J. Am. Chem. Soc.,* 1995, **117**, 2896-2899.
40. K. Weber, L. Hockett, S. Creager, *J. Phys. Chem. B*, 1997, **101**, 8286-8291.
41. F. Chen, X. Li, J. Hihath, Z. Huang, N. Tao, *J. Am. Chem. Soc.*, 2006, **128,** 15874-15881.
42. William B. Davis, Walter A. Svec, Mark A. Ratner & Michael R. Wasielewski, *Nature,* 1998, **396**, 60-63.
43. H. D. Sikes, J. F. Smalley, S. P. Dudek, A. R. Cook, M. D. Newton, C. E. D. Chidsey, S. W. Feldberg, *Science*, 2001, **291**, 1519-1523.
44 F. Giacalone, J. L. Segura, N. Martin, D. M. Guldi, *J. Am. Chem. Soc.*, 2004, **126**, 5340-5341.
45 M. U. Winters, E. Dahlstedt, H. E. Blades, C. J. Wilson, M. J. Frampton, H. L. Anderson, B. Albinsson, *J. Am. Chem. Soc.*, 2007, 129, 4291-4297.
46 G. Sedghi, K. Sawada, L. J. Esdaile, M. Hoffmann, H. L. Anderson, D. Bethell, W. Haiss, S. J. Higgins, R. J. Nichols, *J. Am. Chem. Soc.*, 2008, **130**, 8582–8583
47 F. D. Lewis, R. L. Letsinger, M. R. Wasielewski, *Acc. Chem. Res.*, 2001, **34,** 159-170.
48 D. B. Hall, R. E. Holmlin, J. K. Barton, *Nature*, 1996, **382,** 731-735.
49 D. Porath, A. Bezryadin, S. D. Vries, C. Dekker, *Nature*, 2000, **403**, 635-638.
50 H.-W. Fink, C. Schçneberger, *Nature*, 1999, **398**, 407-410.

51 M. D. Purugganan, C. V. Kumar, N. J. Turro, J. K. Barton, *Science*, 1988, **241,** 1645-1649.
52 C. J. Murphy, M. R. Arkin, Y. Jenkins, N. D. Ghatlia, S. H. Bossmann, N. J. Turro, J. K. Barton, *Science*, 1993, 262, 1025-1029.
53 P. Fromherz, B. Rieger, *J. Am. Chem. Soc.*, 1986, **108**, 5361-5362.
54 A. M. Brun, A. Harriman, *J. Am. Chem. Soc.*, 1992, **114**, 3656-3660.
55. Beratan, D. N.; Onuchic, J. N.; Winkler, J. R.; Gray, H. B. *Science*, 1992, **258**, 1740-1741.
56 H.-B. Kraatz, *Macromol. Symp.*, 2003, **196**, 39-44.
57 M. M. Galka, H.-B. Kraatz, *ChemPhysChem*, 2002, **3**, 356-359.
58 S. K. Dey, Y. T. Long, S. Chowdhury, T. C. Sutherland, H. S. Mandal, H. B. Kraatz, *Langmuir*, 2007, **23**, 6475-6477.
59. Tomoyuki Morita and Shunsaku Kimura *J. Am. Chem. Soc.*, 2003, **125**, 8732–8733.
60. T. A. Zeidan, Q. Wang, T. Fiebig, F. D. Lewis, *J. Am. Chem. Soc.*, 2007, **129**, 9848-9849.
61. M. Wielopolski, A. Molina-Ontoria, C. Schubert, J. T. Margraf, E. Krokos, J. Kirschner, A. Gouloumis, T. Clark, D. M. Guldi, N. Martín *J. Am. Chem. Soc.*, 2013, **135**, 10372–10381.
62. K. Terada, H. Nakamura, K. Kanaizuka, M. Haga, Y. Asai, T. Ishida *ACS Nano*, 2012, **6**, 1988–1999.
63. (a) R. L. McCreery, *Chem. Rev.*, **2008**, *108*, 2646-2687. (b) A. J. Bergren, R. L. McCreery, *Annu. Rev. Anal. Chem.*, 2011, **4**, 173-195. (c) J. J. Warren, M. E. Ener, A. Vlček Jr., J. R. Winklera, H. B. Graya, *Coord. Chem. Rev.*, 2012, *256*, 2478-2487. (d) C. Schubert, J. T. Margraf, T. Clark, D. M. Guldi, *Chem. Soc. Rev.*, 2015, DOI**:** 10.1039/C4CS00262H. (e) O. S. Wenger, *Chem. Soc. Rev.*, 2011, **40**, 3538-3550.
64. R. A. Malak, Z. Gao, J. F. Wishart, S. S. Isied *J. Am. Chem. Soc.*, 2004, **126**, 13888–13889.
65. L. Luo, S. H. Choi, C. D. Frisbie, *Chem. Mater.* 2011, **23,** 631-645.
66. G. Wang, T.-W. Kim, T. Lee, *J. Mater. Chem.* 2011, **21**, 18117-18136.
67. R. L. Mccreery, H. Yan, A. Bergren J. *Phys. Chem. Chem. Phys.* 2013, **15**, 1065.
68. N. Tuccitto, V. Ferri, M. Cavazzini, S. Quici, G. Zhavnerko, A. Licciardello, M. A. Rampi *Nature Mater.* 2009, 8, 41–46.
69. H. Vazquez, R. Skouta, S. Schneebeli, M. Kamenetska, R. Breslow, L. Venkataraman, M. S. Hybertsen, *Nature Nanotech.,* 2012, **7**, 663-667.
70. M. S. Inkpen, T. Albrecht, N. J. Long, *Organometallics,* 2013, **32**, 6053-6060.
71. M. Wanunu, A. Vaskevich, A. Shanzer, I. Rubinstein, *J. Am. Chem. Soc.,* 2006, **128**, 8341-8349.
72. J. Choudhury, R. Kaminker, L. Motiei, Ruiter, G. de M. Morozov, F. Lupo, A. Gulino, M. E. van der Boom, *J. Am. Chem. Soc.,* 2010, **132**, 9295-9297.
73 (*a*) P. R. Andres, U. S. Schubert, *Adv. Mater.*, 2004, **16**, 1043-1068. (*b*) W. Xue, B.-Y. Wang, J. Zhu, W,-X, Zhang, Y.-B. Zhang, H.-X. Zhao, X.-M. Chen, *Chem. Commun.*, 2011, **47**, 10233-10235. (*c*) H. Maeda, M. Hasegawa, T. Hashimoto, T. Kakimoto, S. Nishio, T. Nakanishi, *J. Am. Chem. Soc.*, 2006, **128**, 10024-10025. (*d*) X. Zhang, Z.-K. Chen, K. P. Loh, *J. Am. Chem. Soc.*, 2009, **131**, 7210-7211.
74 (*a*) M. S. Strano, C. A. Dyke, M. L. Usrey, P. W. Barone, M. J. Allen, H. Shan, C. Kittrell, R. H. Hauge, J. M. Tour, R. E. Smalley, *Science*, 2003, **301**, 1519-1522. (*b*) K. Gong, F. Du, Z. Xia, M. Durstock, L. Dai, *Science*, 2009, **323**, 760-764. (*c*) O. Stephan, P. M. Ajayan, C. Colliex, Ph. Redlich, J. M. Lambert, P. Bernier, P. Lefin, *Science*, 1994, **266**, 1683-1685.
75 J. Roncali, *Chem. Rev.*, 1992, ***92***, 711-738.
76 S. Hou, C. C. Harrell, L. Trofin, P. Kohli, C. R. Martin *J. Am. Chem. Soc.* 2004, **126**, 5674-5675.
77 D. S. Lawrence, T. Jiang and M. Levett, *Chem. Rev.* 1995, **95**, 2229-2260.
78 (a) T. Kambe, R. Sakamoto, K. Hoshiko, K. Takada, M. Miyachi, J.-H. Ryu, S. Sasaki, J. Kim, K. Nakazato, M. Takata and H. Nishihara, *J. Am. Chem. Soc.,* 2013, **135**, 2462-2465. (b) T. Kambe, R. Sakamoto, T. Kusamoto, T. Pal, N. Fukui, T. Shimojima, Z. Wang, T. Hirahara, K. Ishizaka, S. Hasegawa, F. Liu and H. Nishihara, *J. Am. Chem. Soc.,* 2014, **136**, 14357–14360. (c) R. Matsuoka, R. Sakamoto, T. Kambe, K. Takada, T. Kusamoto and H. Nishihara, *Chem. Commun.*, 2014, **50**, 8137–8139. (d) R. Sakamoto, K. Hoshiko, Q. Liu, T. Yagi, T. Nagayama, S. Kusaka, M. Tsuchiya, Y. Kitagawa, W.-Y. Wong and H. Nishihara, *Nat. Commun.*, 2015, **6**, 6713. (e) R. Matsuoka, R. Toyoda, R. Sakamoto, M. Tsuchiya, K. Hoshiko, T. Nagayama, Y. Nonoguchi, K. Sugimoto, E. Nishibori, T. Kawai and H. Nishihara, *Chem. Sci.*, 2015, DOI: 10.1039/C5SC00273G. (f) K. Hoshiko, T. Kambe, R. Sakamoto, K. Takada and H. Nishihara, *Chem. Lett.* **2014**, *43*, 252–253.
79 (*a*) R. G. Ding, G. Q. Lu, Z. F. Yan, M. A. Wilson , *J. Nanosci. Nanotechnol.*, 2001, **1**, 7-29; (*b*) R. H. Baughman, A. A. Zakhidov, W. A. de Heer, *Science*, 2002, **297**, 787-792.
80 H. Shirakawa, *Angew. Chem. Int. Ed.*, 2001, **40**, 2574-2580.
81 K. Malmos, J. Iruthayaraj, S. U. Pedersen and K. Daasbjerg, J. Am. Chem. Soc., 2009, 131, 13926-13927.
82 J. Pinson, F. Podvorica, *Chem. Soc. Rev.,* 2005, **34**, 429-439.
83 J. K. Kariuki, M. T. McDermott, *Langmuir,* 2001**, 17***,* 5947-5951.
84 (a) C. Wang, A. S. Batsanov, M. R. Bryce, S. Martín, R. J. Nichols, S. J. Higgins, V. M. García-Suárez and C. J. Lambert, *J. Am. Chem. Soc.*, 2009, **131**, 15647–15654. (b) G. Sedghi, V. M. García-Suárez, L. J. Esdaile, H. L. Anderson, C. J. Lambert, S. Martín, D. Bethell, S. J. Higgins, M. Elliott, N. Bennett, J. E. Macdonald and R. J. Nichols, *Nat. Nanotech.*, 2011, **6**, 517–523. (c) P. Moreno-García, M. Gulcur, D. Z. Manrique, T. Pope, W. Hong, V. Kaliginedi, C. Huang, A. S. Batsanov, M. R. Bryce, C. Lambert and T. Wandlowski, *J. Am. Chem. Soc.*, 2013, **135**, 12228–12240.

